SPACE TELESCOPE SCIENCE INSTITUTE
Operated for NASA by AURA

**Instrument Science Report WFPC2 2009-07**

# Red Leak Characterization for the WFPC2 UV Filters

P. L. Lim, M. Chiaberge, J. Biretta, and D. Di Nino
December 18, 2009

**ABSTRACT**

*We characterize the red leaks for all eight WFPC2 UV filters (F122M, F160BW, F170W, F185W, F218W, F250W, F300W, and F336W). We crossed each UV filter with three broad band optical filters (F450W, F606W, and F814W) in order to isolate different spectral regions in the red leak. We observed 15 Mon, an O7Ve-type star, using five different pointings to position the star at different locations on three WFPC2 chips (PC1, WF2, and WF3) to study possible filter inhomogeneities. We also observed g Gem, a K4III-type star, with WF3 as a follow-up to further study selected filters. Our results for F160BW, F170W, F300W, and F336W show good agreement (within 20%) between the observed off-band count rates and those predicted by SYNPHOT. Filters F185W, F218W, and F255W showed significant discrepancies between the observed and predicted values (20% to 250%); we derived new throughput curves for these filters, and delivered them to CDBS. The F122M filter shows evidence for a long-term throughput decline and will require additional studies beyond the scope of this report.*

## 1. Introduction

As a part of the WFPC2 close-out calibration plan, we characterized the in-flight red leak properties for the whole set of eight UV filters – F122M, F160BW, F170W, F185W, F218W, F255W, F300W, and F336W. The presence of substantial off-band flux in the red part of the spectrum could pose significant problems in analyzing data of red sources and appropriate corrections must be taken into account. Observers mainly rely on

Operated by the Association of Universities for Research in Astronomy, Inc., for the National Aeronautics and Space Administration

SYNPHOT for such red leak corrections. Hence, it is important that the throughput curves correctly describe the filter red leaks.

The red leak regions of the SYNPHOT throughput curves available (prior to our new CDBS deliveries) were based on pre-launch lab calibrations. Although the tables were updated with on-orbit observations, each was only scaled with a constant factor with no change to the shape of the spectrum and only in-band flux accuracy was studied (Baggett et al. 1997). In addition, aging might also play a role in modifying the throughputs (e.g., F122M; see Section 5.6.1). Therefore, checking the red leak properties of the UV filters is an important part of the WFPC2 closeout calibration plan.

For this project, we observed a bright O7Ve-type star, 15 Mon ($m_V$ = 4.68 mag). This choice is motivated by the fact that its brightness is desirable for cross-filter observations and that its spectrum is smooth and well-characterized by previous HST STIS/ACS observations. The star was also used in a similar ACS calibration program (Chiaberge & Sirianni 2007). We obtained observations of 15 Mon in five different chip locations in anticipation of possible filter inhomogeneities (and charge transfer efficiency, CTE, losses), which could compromise our results.

We also included an additional red star, g Gem, to improve the red leak calibration for select filter pairs. It is a K4III-type star ($m_V$ = 4.884 mag) and also a spectroscopic binary. Its selection was based on its similar brightness compared to 15 Mon, wavelength peak in the red, availability of spectrum in SYNPHOT, and availability during observation windows. For simplicity, we only used WF3 chip with the star located near the amplifier.

We describe our observations and data reduction in Sections 2 and 3, respectively. We present our analysis and results in Sections 5 and 6. Finally, we summarize our findings in Section 7.

## 2. Observations

The data were taken as part of two calibration proposals, 11036 and 11327 (PI: M. Chiaberge). We observed 15 Mon, an O7Ve-type star used in the ACS red leak calibration (Chiaberge & Sirianni 2007), on 4 Sep. 2007, 31 Dec. 2007, 12-14 Jan. 2008, and 3 Sep. 2008. The star is an astrometric and spectroscopic multiple star system (Gies et al. 1997). One component is unresolved with WFPC2 and already accounted for in the photometry and spectral characteristics of 15 Mon. The other component is resolved and located ~3″ away from the primary -- it is well outside our aperture photometry radius, and hence does not affect our flux measurements.

We obtained exposures for each UV filter crossed with three optical broad band filters – F450W, F606W, and F814W; hereafter, the latter are collectively referred to as the "red" filters. Such cross-filter observations enable the isolation of three different red leak regions in the UV filter throughputs, as illustrated in Figure 1 – Normalized passband for F170W (purple) is overlaid with red leak regions covered by F450W (blue), F606W (green), and F814W (red). Therefore, most of our detected counts would originate from the respective red leak spectral regions shown.

**Figure 1:** Normalized passband for F170W (purple), overlaid with red leak regions covered by F450W (blue), F606W (green), and F814W (red).

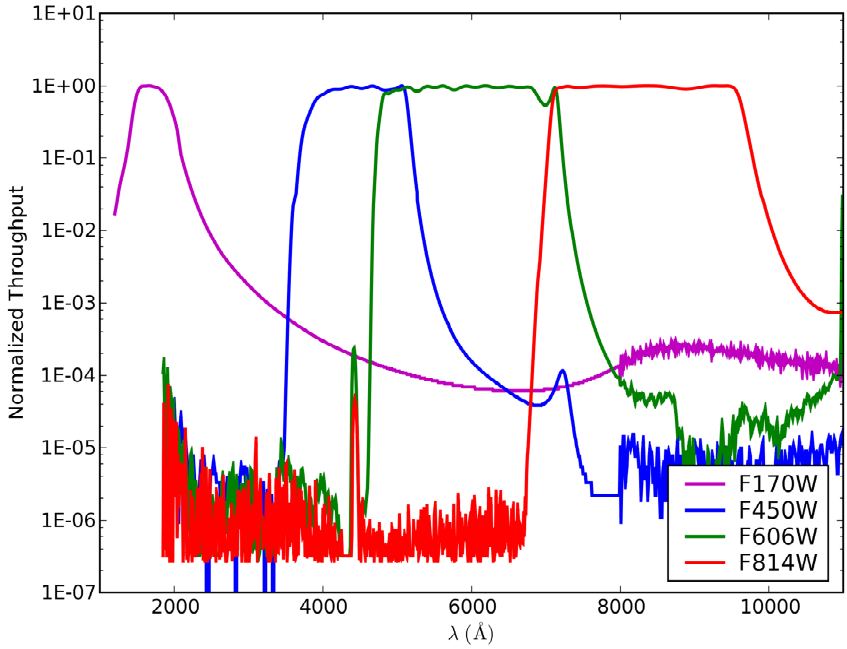


We used five different pointings across the WFPC2 field of view (FOV) to study possible filter inhomogeneities (comparing the same position on different chips) and to assess the impact of CTE losses (comparing different positions on each chip). Each pointing is named after the chip (e.g., WF3), followed by "c" (center) or "s" (side). Due to the presence of the WF4 anomaly (Biretta & Gonzaga 2005), that chip was excluded from observations. Table 1 relates the pointing names to the apertures used. Figure 2 illustrates their approximate positions on WFPC2 FOV and relative to the amplifier readout directions.

For each filter pair, positioning the star at different locations in the FOV samples the different physical surfaces of the filters. Filter inhomogeneities could be disentangled from CTE effects by comparing the stellar fluxes measured from a pair of pointings with equidistance from their respective amplifiers (e.g., WF2c and WF3c), provided that the

CTE loss is independent of the chip used, which is a standard assumption in WFPC2 CTE analysis because the chip used is not a part of the correction formulae (e.g., Dolphin 2004).

In addition, we observed g Gem, a K4III-type star, on 12 Jan. 2009 for select UV filters (F122M, F170W, F185W, F218W, and F255W) that needed more accurate red leak characterizations and for checking against the presence of blue leaks in the "red" filters (see Section 4.2). Only the WF3s pointing was used in order to minimize CTE losses, as its location is near the readout amplifier. Data from g Gem are complementary to those from 15 Mon for the studies of unexpected throughput gaps in F185W, F218W, and F255W (see Sections 5.5, 5.6.3, and 5.6.4) and the throughput change in F122M (see Section 5.6.1), while using the well-behaved F170W as a control.

**Table 1:** Pointings and apertures used for red leak characterization in UV filters.

| Pointing | Aperture | POS-TARG (″) |
|---|---|---|
| PC1c | PC1-FIX | None |
| WF2c | WF2 | None |
| WF2s | WF2 | 28.47, -24.27 |
| WF3c | WF3 | None |
| WF3s | WFALL | None |

**Figure 2:** Aperture positions on the WFPC2 chips. Arrows are chip readout directions. Stars show the approximate pointing locations; their names as labeled. WF4, labeled in parenthesis, is excluded from our observations.

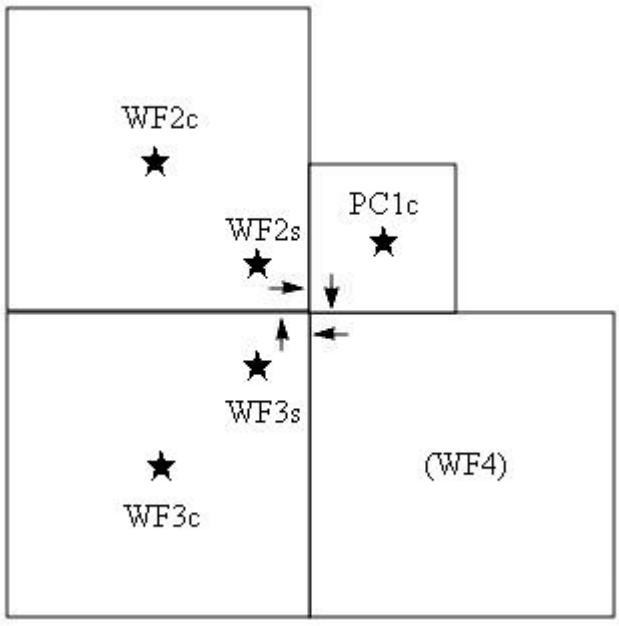

## 3. Data Reduction

We reduced our data via the standard *calwp2* pipeline (WFPC2 Data Handbook by Baggett et al. 2002; hereafter DHB). We used the corresponding "red" filter flat-field, as tabulated in Table 2 (Koekemoer, Biretta, & Mack 2002), because the bulk of the flux was expected to come from the red leak region of each UV filter. For the 15 Mon observations and most of the g Gem exposures, we used the IRAF task *crrej* to combine two similar exposures for cosmic ray removal. For g Gem single exposures, where necessary, we cleaned those using IRAF tasks *cosmicrays* and *fixpix*, making sure that their PSFs were unaltered.

**Table 2:** The flatfield reference files used for cross-filter data for red leak characterization.

| Reference File Name | "Red" Filter | USEAFTER Date |
|---|---|---|
| m3c1004bu | F450W | 1996-10-30 |
| m3c1004ku | F606W | 1996-10-30 |
| m3c10050u | F814W | 1996-10-30 |

According to Part II Chapter 5.2 of DHB, we applied the pixel area correction using *f1k1552bu.r9h* (from CDBS) and 34$^{th}$ row correction (Anderson & King 1999) to the images.

For 15 Mon, F300W×F450W and F336W×F450W exposures were saturated due to overlapping in-band fluxes and thus excluded from analysis. F300W×F814W (WF2c and WF2s), F336W×F606W (WF2c), and F336W×F814W (all pointings) were also saturated in the initial observations, but were later re-observed. F300W×F814W (PC1c, WF3c, and WF3s) and F336W×F606W (WF2s and WF3c) had single-pixel saturation, which did not significantly affect the results, and therefore were still used for analysis.

## 4. Possible sources of error

Characterization of red leak by crossing UV with broad band optical filters could be compromised by contamination in the UV filters or blue leak in the optical ones. Therefore, we explore their potential impacts on our cross-filter observations in Sections 4.1 and 4.2, respectively.

### 4.1. Contamination

Throughputs in the UV could decrease over time due to molecular contaminants adhering to the CCD windows (WFPC2 Instrument Handbook by McMaster, Biretta, et al. 2008; hereafter IHB). To minimize this effect, WFPC2 underwent monthly decontaminations, where periodic warming would diminish the contaminants. There is also long-term evolution in UV throughputs (DHB Part II Section 5.2.1).

Volatile contaminants (that could be removed by decontamination) should not affect our cross-filter observations because the primary contributor of our observed counts is from the red leak region and not UV. Meanwhile, any long-term filter throughput or chip QE evolution is expected only to be a few percent, well below the accuracy level of 20% that we could reach with the observations (see Section 5.4).

For instance, the 15 Mon exposures were taken from just after, to about a month after, their respective decontaminations on 4 Sep. 2007, 14 Dec. 2007, and 7 Aug. 2008. Regardless, their data provided similar photometry results, supporting our statements above. Contamination effects would be even less significant for g Gem, as more of its flux falls on the red leak region than 15 Mon.

## 4.2. Blue Leaks

The blue cutoff in each of the "red" crossing filter throughput curves is sharp and has sensitivity that quickly drops down to $\lesssim 10^{-6}$ (prior to convolution with other HST elements). However, we could not rule out the possibility that some flux bluer than the cutoff wavelength (i.e., blue leak) may be detected in our observations, since the UV filter passbands would overlap with any blue leak in the "red" filters.

For a very blue source like 15 Mon, blue leak in the "red" filters could be significant. If the blue leak has evolved over time, then the red leak calibration could be compromised, as the extra flux from blue leak could be mistaken to be from the red instead. Moreover, blue leak could be non-uniform across the UV passbands (i.e., for a particular "red" filter, the effect could be more prominent in crossing with a certain UV filter but not the others). In such scenarios, a red giant like g Gem would provide more accurate red leak characterizations (e.g., Sections 5.6.4 and 5.6.5).

# 5. Analysis and Results

Sections 5.1 and 5.2 describe our methods to obtain photometry values and CTE corrections. Their results are given in detail in Appendix A, including reduced cross-filter images, plots of aperture corrections, and a table of raw magnitudes, corrections, and final observed count rates. The rest of the subsections, titles of which are self-explanatory, detail our red leak and related studies on the mentioned results.

## 5.1. Photometry

We performed aperture photometry using the IRAF task *phot*. The sky background was measured using *centroid* fitting in an annulus with inner radii 87 and 40 pixels from the star, with widths 152 and 30 pixels, for PC and WF, respectively. These sky radii were chosen such that the resolved companion of 15 Mon was excluded. Initial star positions

were visually determined for each chip and then used for re-centering within 10 pixels (the actual position could shift due to jitter, etc.) using the IRAF task *center*. Gain and read noise values from Table 4.2 in IHB were used to estimate the photometric error, for which we followed the WFPC2 Photometry Tutorial (Gonzaga 2002).

Due to the irregular PSF shape in cross-filter images (caused by de-focus when a second filter is introduced), we were unable to apply standard aperture corrections. Therefore, we used an alternate method described below.

We used two aperture radii – 0.5″ (11 pixels for PC; 5 pixels for WF) and 2″ (43.5 pixels for PC; 20 pixels for WF). The larger 2″ aperture includes most of the stellar flux (>99%), but for the faint images it can be affected by noise fluctuations. On the other hand, the smaller aperture includes a smaller fraction of the total flux and requires aperture correction. We derived the aperture correction for each filter pair and pointing by subtracting the 0.5″ aperture magnitude from that of 2″. Although we were unable to recover 100% of the flux in the larger aperture, this approach is sufficient for the accuracy level required.

Our aperture correction restores the 0.5″ aperture photon to that of the 2″. The 0.5″ values are necessary to identify cases with unreliable larger aperture counterparts, as stated below. Such cases are picked out by comparing the two apertures for all filter pairs (see Figure A7 and Figure A8). The 0.5″ aperture is also used for CTE corrections (see Section 5.2).

For the 15 Mon exposures, we applied the aperture correction derived for the filter pair F218W×F450W to the observations taken with F218W×F606W and F218W×F814W (due to excessive noise in the 2″ aperture photometry for the latter two). By comparing all the aperture corrections derived with this method, we are confident that the value derived from the first filter pair could be applied to the other two without significant loss of accuracy (i.e., wavelength dependency of a PSF is a low level effect in our crossed-filter observations). Similarly, we applied corrections obtained with F255W×F450W to F255W×F606W and F255W ×F814W. For g Gem, we applied the value for F218W×F814W to F218W×F450W.

## 5.2. CTE Losses

For the images in which the star is located at the center of the chip (i.e., far from the amplifier), count loss due to charge transfer inefficiency (CTI, as opposed to CTE) significantly impacts our measurements. As prescribed by Dolphin (2004), we applied CTE correction formulae to these data derived using a 0.5″ aperture.

Note that the aperture correction outlined in Section 5.1 also corrects for part of the CTI. The larger aperture is less impacted than the smaller one due to the properties of CTI-inducing "traps." Some of the trapped charges are released on a timescale much shorter than the readout time and are recovered during readout but appear shifted on the image (i.e., in pixels not corresponding to the actual target position), which are known as CTE tails (Cawley et al. 2001). Hence, our aperture correction recaptures the charges in the CTE tails between 0.5″ and 2″. However, trapped charges released on a longer timescale cannot be recovered. To avoid overcorrecting for CTE loss in such cases, we used the average of the counts (also corrected for aperture) obtained with and without CTE correction (calculated from 0.5″ measurements, as stated above) as our observed value.

We applied the CTE corrections, as described, to 15 Mon exposures with the star located at the center of the chips. No such correction is needed for data (for both 15 Mon and g Gem) in which the star is located at the "side" position, which is close to the amplifier.

## 5.3. Filter Inhomogeneity and CTE

In order to check for filter inhomogeneities, we calculated the residuals of the stellar fluxes (in units of magnitude) measured for 15 Mon located at different positions and on different chips. We used the 0.5″ aperture photometry results and plotted the residuals against the total counts in each filter pair in Figure 3. For example, "Δmag (WF2c - WF3c)" is the difference between the instrumental magnitudes of the star measured at the centers of the WF2 and WF3 chips. This difference is then plotted against the total counts derived in WF2c; similarly, "Δmag (WF2s - WF3s)" is plotted against WF2s. Since the star is equidistant from the amplifier on both chips, no CTE correction is necessary. The UV filters used (e.g., "122" for F122M) are labeled on top of the corresponding data points. The colors blue, olive green, and red represent crossing the UV filter with F450W, F606W, and F814W, respectively. As expected, lower total counts have larger photometry errors.

Interestingly, Figure 3a shows larger residuals for lower total counts; whereas, Figure 3b shows consistent count rates between WF2s and WF3s regardless. It seems unlikely that this behavior in Figure 3a is caused by filter inhomogeneity – it would be surprising if F185W, F218W, and F255W all had very similar inhomogeneities between the WF2c and WF3c aperture locations. It appears more likely that the observed effect is related to CTI – at the center of the chip with a substantial number of transfers, CTI would indeed affect the faint stars more than the brighter ones. The observed trend could be explained if the CTE is different in the two chips. Chip-dependent CTE had been suggested in WFPC2 ISR 05-01 (Biretta & Kozhurina-Platais 2005) based on the studies of hot pixel tails.

In addition, in our other plots comparing the count rate measurements at different positions on the chips, we did not find any trend with the filter pairs. Despite the large measurement uncertainties, our findings showed no evidence of filter inhomogeneity effects in our data. From the observed scatters for the highest total counts ($10^4$ to$10^5$ DN), where statistical errors are small, we estimate the upper limit of any filter inhomogeneity derivable from our data to be ~5%.

**Figure 3:** Comparison of observed 15 Mon count rates (in mag) for different pointings. Count rates are from a 0.5″ aperture. The X-axis shows the total counts (in log DN) for the same aperture radius. No CTE correction is performed (see text). In-plot labels indicate the UV filter (e.g., "122" for F122M). Blue, olive green, and red points represent the "red" filters F450W, F606W, and F814W, respectively, which are crossed with the corresponding UV filters.

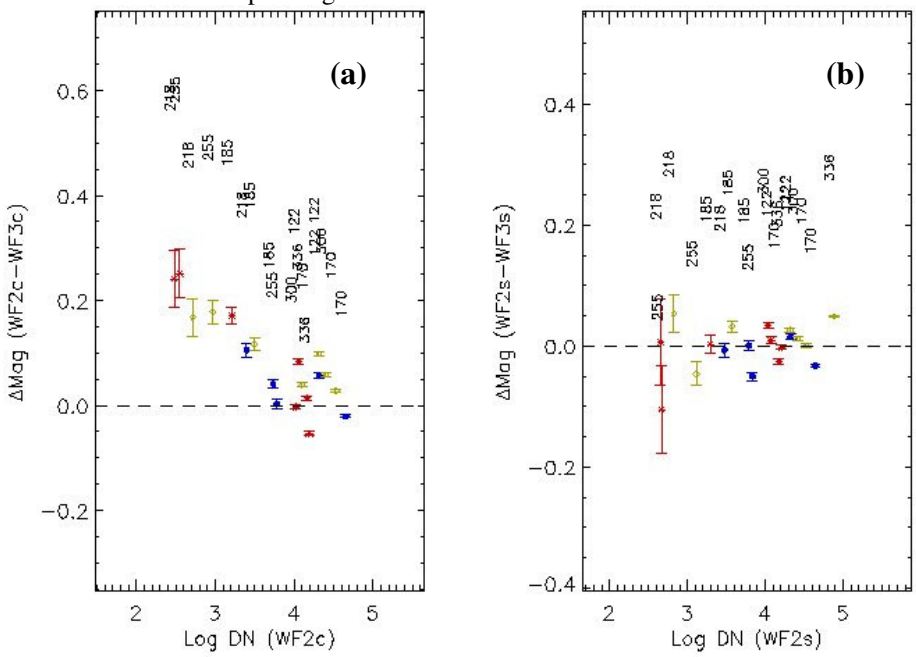


## 5.4. Comparison with SYNPHOT

We used the IRAF task *calcphot* to obtain the predicted count rates from SYNPHOT in DN $s^{-1}$ for each filter pair and chip. We did not include contamination modeling as it is insignificant in the red leak regime (see Section 4.1). For 15 Mon, we used the Bruzual atlas spectrum for an O7V-type star[a] renormalized to 4.68 mag in *V*-band. For g Gem, we used its Bruzual-Persson-Gunn-Stryker atlas spectrum[b] (Gunn & Stryker 1983) renormalized to 4.884 mag in *V*-band[c]. The predicted count rates are tabulated in Appendix B.

[a] ftp://ftp.stsci.edu/cdbs/grid/bz77/bz_2.fits
[b] ftp://ftp.stsci.edu/cdbs/grid/bpgs/bpgs_150.fits
[c] Magnitude value is taken from SIMBAD (http://simbad.u-strasbg.fr).

For comparison with photometry results, we define $\Delta f$ as

$$\Delta f = (f_{obs} - f_{syn}) / f_{syn}\,, \qquad (1)$$

where $f_{obs}$ and $f_{syn}$ are observed and predicted count rates, respectively. Percentage values of $\Delta f$ are shown in Figure 4 to Figure 6. For each UV filter, crossing with F450W, F606W, and F814W are represented by blue circle, olive green diamond, and red asterisk, respectively. The $\Delta f$ errors shown are statistically propagated from photometry results. For a star measured at the center of the chip (e.g., WF3c), the count rate used is the average of those corrected and uncorrected for CTE loss (see Section 5.2). Otherwise, no CTE correction is applied, as explained above. Our goal is to determine the filter red leaks to an accuracy of 20%; hence, we have indicated $|\Delta f| \lesssim 20\%$ limits in the figures. Given that the transmission in red leak is several magnitudes lower than in-band and the difficulties in measuring the red leaks, 20% was deemed to be sufficient accuracy.

Detailed discussions for each UV filter are in Sections 5.6.1 to 5.6.5. From Figure 4 to Figure 6, it was evident that filters F122M, F185W, F218W, and F255W did not meet our goal for 20% accuracy of the red leak calibration. For the shortest wavelength filter, F122M, we believe this is attributable to long-term contamination issues and resulting far-UV throughput loss (see Section 5.6.1). For the other three filters, we discovered "gaps" or wavelength ranges (in the red leak regions only) where the SYNPHOT throughput curves appear to be artificially set to zero transmission. Note that these “gaps” were not present in the spectral transmission curves given in the original WFPC2 Science Calibration Report (Trauger et al. 1993); unfortunately, the tables used to construct those curves were unavailable to us.

## 5.5. “Gap” Corrections

In order to reconcile predicted and observed values for F185W, F218W, and F255W, we empirically completed their SYNPHOT throughput curves. Firstly, we divided the “gap” in each affected UV filter into wavelength segments corresponding to each of the “red” filter bandpass, such that each segment represents where the bulk of the flux would fall for each filter pair. Then, each segment (i.e., filter pair) was roughly divided at the “red” filter pivot wavelength, such that 15 Mon would be the main flux contributor of the short-ward sub-segment (hereafter bin) and g Gem the long-ward. In total, there were 6, 4, and 2 bins for F185W, F218W, and F255W, respectively, based on the nature of their “gaps.”

The binning method described above is illustrated in Figure 7 – A segment for F185W×F606W is divided into two bins: (a) 5170 Å $\leq \lambda <$ 6300 Å; and (b) 6300 Å $\leq \lambda <$ 7200 Å. The plotted count distributions represent the convolutions of the F606W passband (on WF3) with 15 Mon (shaded blue) and g Gem (shaded red), respectively. F185W is unable to be included in the plot due to its “gap” but the filter is still

**Figure 4:** Comparison for 15 Mon count rates between observations and SYNPHOT predictions. The star is located at the center of the chip, so the observed count rate is the average of those corrected and uncorrected for CTE loss (see Section 5.2). Dotted lines mark the ±20% cutoff.

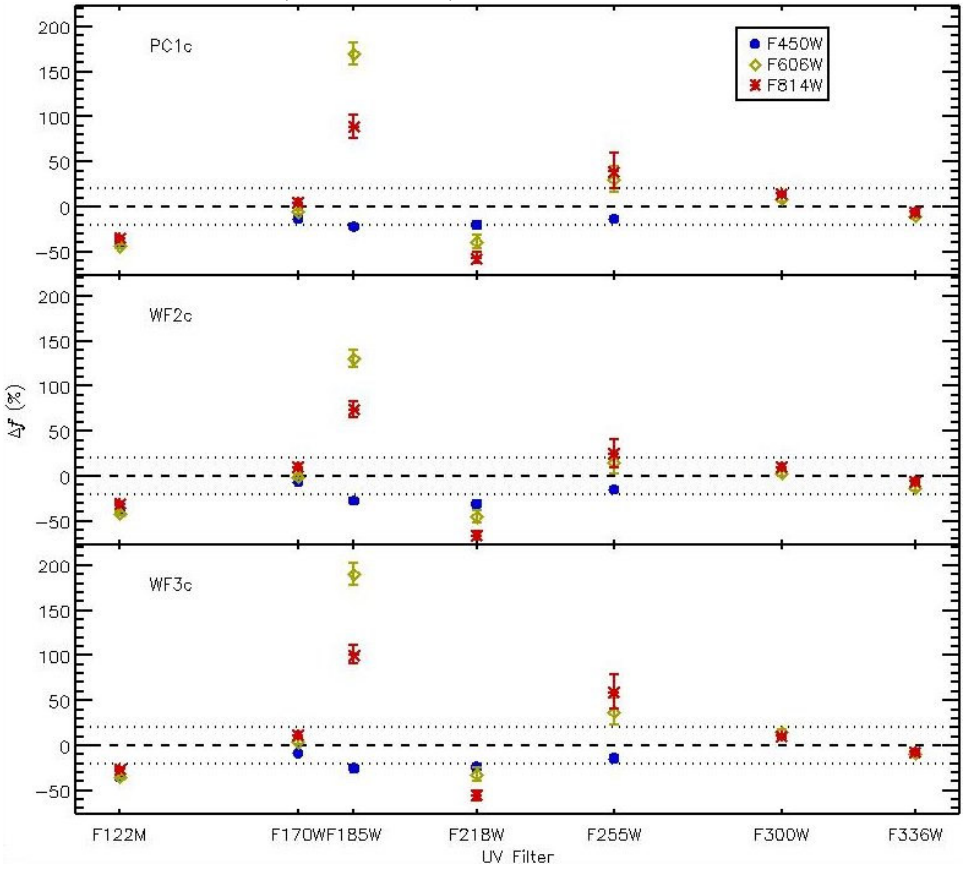


**Figure 5:** Comparison for 15 Mon count rates between observations and SYNPHOT predictions. The star is located at the side of the chip, so no correction for CTE loss is necessary. Dotted lines mark the ±20% cutoff.

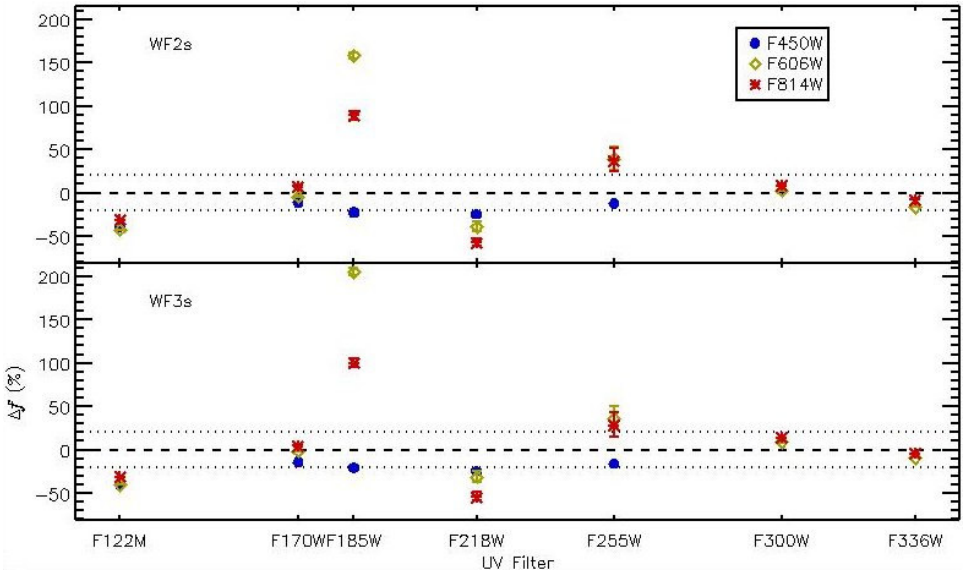

**Figure 6:** Comparison for g Gem count rates between observations and SYNPHOT predictions. The star is located at the side of the chip, so no correction for CTE loss is necessary. Dotted lines mark the ±20% cutoff.

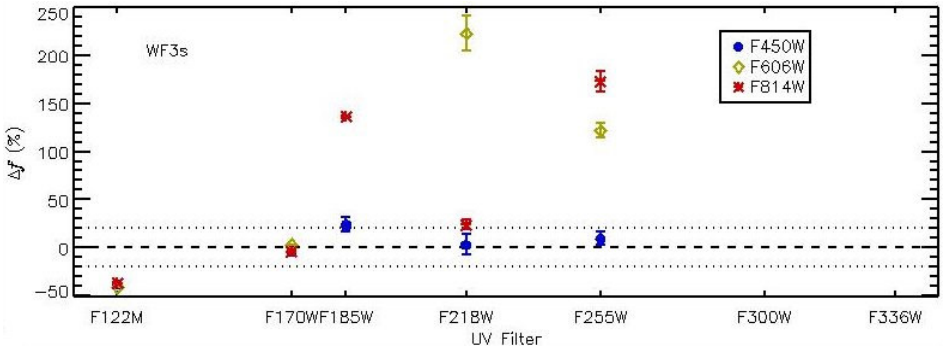


considered in our gap correction method. For clarity, the overlap between 15 Mon and g Gem is shaded in green. This figure shows that the bulk of red leak in the F606W passband for 15 Mon comes from bin (a); similarly, bin (b) for g Gem. All filter pairs start out with this same concept but the bin boundaries are empirically adjusted, as described below.

For each bin, we iteratively adjusted the transmission value (and bin boundaries, where necessary) until $|\Delta f| \lesssim 20\%$ for all related observations (spanning multiple "red" filters and both stars for the UV filter). We also removed throughput digitization effects via boxcar smoothing for $\lambda \gtrsim$ 10,000 Å (the resulting count rate changes are only a few percent; <1% for 15 Mon and g Gem). For simplicity, we used only data with WF3s pointing. Each newly obtained UV throughput was compared to the one previously available in SYNPHOT, with contamination modeling, to ensure that its in-band transmission was unchanged. Then, we delivered the corrected throughputs to CDBS, following the procedures outlined in CDBS TIR 08-01 (Diaz & Cracraft 2008).

Table 3 tabulates our "gap" correction results for F185W, F218W, and F255W. The filter pairs and stars are used as a basis to define the bins, as explained above. Each wavelength bin is defined by the limits $\lambda_1 \leq \lambda < \lambda_2$. The new transmission value across the bin is $T_{new}$, where applicable; if not stated, the existing transmission is retained. For a filter pair and star, the agreements between observations and predictions for before and after the corrections are $\Delta f$ and $\Delta f'$, respectively (see Equation 1).

For F218W and F255W, for which simultaneous agreements for both 15 Mon and g Gem could not be achieved, we only used the latter for corrections because its data were more reliable (see Section 5.6.4).

**Figure 7:** F185W×F606W segment divided into two bins: (a) 5170 Å ≤ λ < 6300 Å; and (b) 6300 Å ≤ λ < 7200 Å. Convolutions of the F606W passband with 15 Mon (shaded blue) and g Gem (shaded red) are calculated for WF3 and gain "7" (F185W is not included in this plot due to its "gap"). For clarity, the overlapping region between both stars is shaded in green.

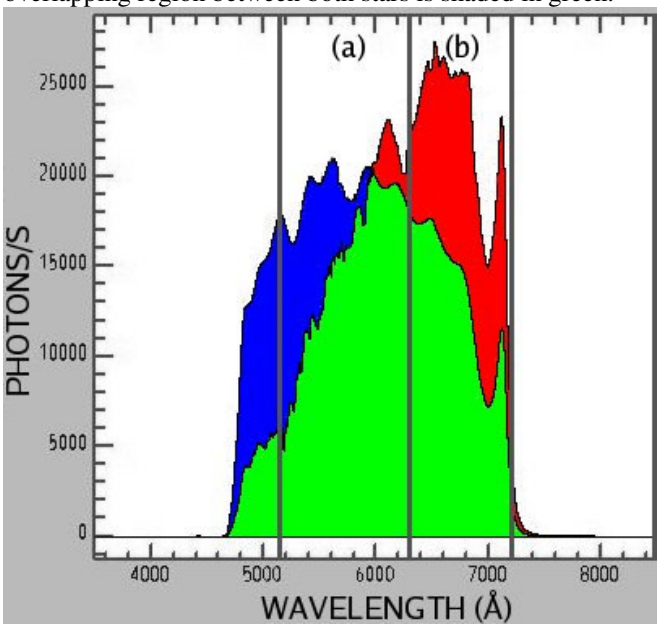


**Table 3:** "Gap" correction results for F185W, F218W, and F255W. Observed data are from WF3s pointing with gain "7." The filter pairs and stars are used as a basis to define the bins (see text). Each bin is constrained by $\lambda_1 \leq \lambda < \lambda_2$, with $T_{new}$ as its new transmission value. The agreements between observations and predictions for a filter pair and star for before and after the corrections are $\Delta f$ and $\Delta f'$, respectively.

| UV Filter | "Red" Filter | Star | $\lambda_1$ (Å) | $\lambda_2$ (Å) | $T_{new}$ | $\Delta f$ (%) [I] | $\Delta f'$ (%) [II] |
|---|---|---|---|---|---|---|---|
| F185W | F450W | 15 Mon | 3800.0 | 4600.5 | $8.560\times10^{-6}$ | -20.6 | -3.7 |
| F185W | F450W | g Gem | 4600.5 | 5170.0 | $4.125\times10^{-6}$ | 23.7 | 3.9 |
| F185W | F606W | 15 Mon | 5170.0 | 6300.0 | $8.000\times10^{-7}$ | 205.2 | -3.5 |
| F185W | F606W | g Gem | 6300.0 | 7200.0 | $3.500\times10^{-6}$ | 230,167.0[III] | 10.7 |
| F185W | F814W | 15 Mon | 7200.0 | 8012.2 | $4.500\times10^{-6}$ | 100.2 | -16.6 |
| F185W | F814W | g Gem | 8012.2 | 9500.0 | $1.000\times10^{-5}$ | 136.0 | -3.0 |
| F218W | F450W | 15 Mon | — | — | — | -24.2 | (-24.2) |
| F218W | F450W | g Gem | — | — | — | 2.9 | 2.9 |
| F218W | F606W | 15 Mon | 5380.0 | 5783.8 | $5.000\times10^{-7}$ | (-31.2) | (-47.1) |
| F218W | F606W | g Gem | 5783.8 | 7300.0 | $3.400\times10^{-7}$ | 222.8 | 0.1 |
| F218W | F814W | 15 Mon | 7300.0 | 8282.4 | $6.000\times10^{-7}$ | (-54.3) | (-58.2) |
| F218W | F814W | g Gem | 8282.4 | 8500.0 | $8.000\times10^{-7}$ | 23.6 | 3.6 |
| F255W | F450W | 15 Mon | — | — | — | -15.9 | (-15.9) |
| F255W | F450W | g Gem | — | — | — | 9.4 | 9.4 |
| F255W | F606W | 15 Mon | — | — | — | (36.4) | (0.4) |
| F255W | F606W | g Gem | 5880.0 | 7300.0 | $6.800\times10^{-7}$ | 121.8 | -1.9 |
| F255W | F814W | 15 Mon | — | — | — | (28.0) | (-36.9) |
| F255W | F814W | g Gem | 7300.0 | 8700.0 | $7.800\times10^{-7}$ | 173.0 | 9.8 |

[I] Values in parenthesis are derived from noise-dominated photometry.

[II] Values in parenthesis are not considered during "gap" corrections. See Section 5.6.4.

[III] Result of unrealistically small predicted count rate for this filter pair and star due to "gap." See Section 5.5.

## 5.6. Results by Filter

In Sections 5.6.1 to 5.6.5, we discuss our findings in detail for each of the eight UV filters. For simplicity, those with similar results are grouped in the same section.

### 5.6.1. F122M

For the F122M filter, we found that the measured count rates in the red leaks are consistently lower ($\Delta f \approx$ -40%) than the SYNPHOT estimates across all pointings and for both stars. To investigate this result further, we carried out an independent check with GRW+70 5824[d], a white dwarf standard star, using a F122M exposure (*ub0pmg05m*) from proposal 11796 taken shortly after the decontamination. We performed standard data reduction and photometry, including geometric, 34$^{th}$-row, aperture (0.1 mag for a 0.5″ aperture), and CTE corrections.

Comparing the observed count rate for GRW+70 5824 with that predicted by SYNPHOT with contamination modeling, we found $\Delta f \approx$ -19%. A post-recovery report following the failure of SIC&DH[e] stated that F122M was found to have count levels ~25% lower than expected (Biretta & Gonzaga 2008; private communications). The 6% discrepancy between the two measurements could arise from the different data reduction methods used. Regardless, it is undeniable that this filter has undergone significant throughput decrease across all wavelengths.

Therefore, we were unable to separate any change in the red leak from the overall throughput change. Correcting for in-band transmission is beyond the scope of this project as our data are tailored for red leak studies. This behavior in F122M shall be addressed in a future report, resources permitting.

### 5.6.2. F160BW

F160BW was expected to have the lowest red leaks among the eight UV filters. SYNPHOT predicted that crossing it with F450W, F606W and F814W would produce 0.8, 1.8, and 0.4 DN s$^{-1}$, respectively, for 15 Mon. For instance, in a F160BW×F606W exposure with 80s exposure time, a total of 144 DN was expected. A 2-pixel aperture on WF should contain 66% of the counts[f], i.e., 95 DN; however, the 2-σ upper limit of our detection is ~40 DN. This indicates that the red leak is even lower than expected.

[d] ftp://ftp.stsci.edu/cdbs/current_calspec/grw_70d5824_stisnic_002.fits
[e] Science Instrument Control & Data Handler; Its Side A failed in September 2008. Then it operated on Side B until its replacement was installed during Servicing Mission 4 in May 2009.
[f] WFPC2 Exposure Time Calculator v4.0 (http://www.stsci.edu/hst/wfpc2/software/wfpc2-etc.html)

To confirm this absence of red leak, we also observed Antares (of M1.5Iab-b spectral type) with WF3s pointing on 5 May 2009. In the combined images of 520s in F160BW×F606W, 300s in F160BW×F814W, and even 820s from stacking the former two, we found no trace of the red primary or its blue companion. As a control, we also examined its F170W×F606W data of 1s and found the red star to be nearly saturated, while the blue star was faint but visible.

Based on the non-detections in cross-filter observations for both 15 Mon and Antares, it is clear that there is effectively no red leak in F160BW. Despite the red leak over-predictions for 15 Mon in SYNPHOT, as mentioned above, they still result in virtually no percentage red leak when the in-band flux is taken into account (see Section 6). Therefore, no modification to the existing F160BW throughput curve is necessary.

### 5.6.3. F185W

The SYNPHOT throughput curve for the F185W filter showed a significant "gap" across the red leak region, i.e., 4720-7990 Å. As discussed in Section 5.5 and tabulated in Table 3, we filled the "gap" with new transmission values based on observations with 15 Mon and g Gem, for which we were able to reduce the maximum $|\Delta f|$ disagreements approximately from 205% to 17% and from $2.3\times10^5$% to 11%, respectively. The newly derived throughput, along with the previously available one, is shown in Figure 8.

We performed additional analysis with the standard calibration star GRW+70 5824 (data reduction similar to that in Section 5.6.1) to investigate the in-band behavior of the filter, which should not be affected by our red leak modifications above. Comparing the observed and SYNPHOT fluxes for the star, we obtained $\Delta f$ values of -0.72% and -0.88% for the existing and the new F185W passbands, respectively. These show that the UV in-band flux is preserved in the new throughput curves and also has not changed significantly since the previous throughput calibration.

### 5.6.4. F218W and F255W

F218W and F255W had "gaps" spanning the spectral regions 5380-6990 Å and 5880-7990 Å, respectively. Akin to F185W, we used the method outlined in Section 5.5 to fill the "gaps" and their results are also tabulated in Table 3. Due to the nature of these "gaps" (i.e., narrower and mainly in the F606W and F814W passbands), we deemed it unnecessary to use cross-filter observations with F450W for such corrections.

In addition, we used only g Gem data to derive the new transmission values and managed to reduce the maximum $|\Delta f|$ disagreements approximately from 223% to 4% and from

**Figure 8:** Previously available (blue dotted line; *wfpc2_f185w_005_syn.fits*) and corrected (red solid line; *wfpc2_f185w_006_syn.fits*) throughputs for F185W.

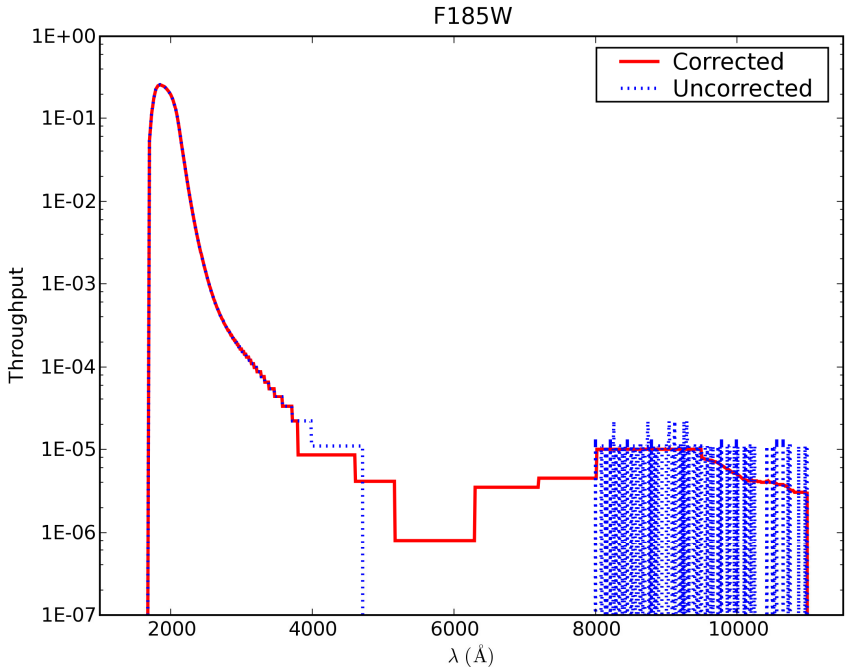


173% to 10%, for F218W and F255W, respectively. The newly derived throughputs, along with the previously available ones, are shown in Figure 9 and Figure 10.

While iteratively adjusting the new red leak transmissions, we were unable to get $\Delta f$ values from 15 Mon and g Gem simultaneously within our ±20% limits. Hence, we decided not to use 15 Mon in our constraints for several reasons. Its detected counts in the related filter pairs were much lower than those for g Gem, resulting in larger photometry errors. For F218W, observed red leak fluxes were lower than predicted (not higher, as one would expect from using a SYNPHOT throughput with "gap"); while for F255W, the observed red leaks were still too low to be consistent with those in g Gem (see Figure 4 and Figure 5). As discussed in Section 4.2, 15 Mon is also more susceptible to any blue leak evolution in the "red" filters. All in all, g Gem would provide a more reliable red leak characterization for F218W and F255W.

Following the "gap" corrections, we performed additional in-band analysis with GRW+70 5824, as detailed in Section 5.6.3. For F218W, the $\Delta f$ values are 0.81% and 0.56% using the existing and the new passbands, respectively; and for F255W, they are 8.1% and 7.6%. These show that our modifications to the red leak transmissions do not significantly affect the in-band UV throughputs, as expected. Since the previous throughput calibrations, F218W in-band has changed very little; however, ~8% increase in F255W might be real but it is beyond the scope of this project.

**Figure 9:** Previously available (blue dotted line; *wfpc2_f218w_006_syn.fits*) and corrected (red solid line; *wfpc2_f218w_007_syn.fits*) throughputs for F218W.

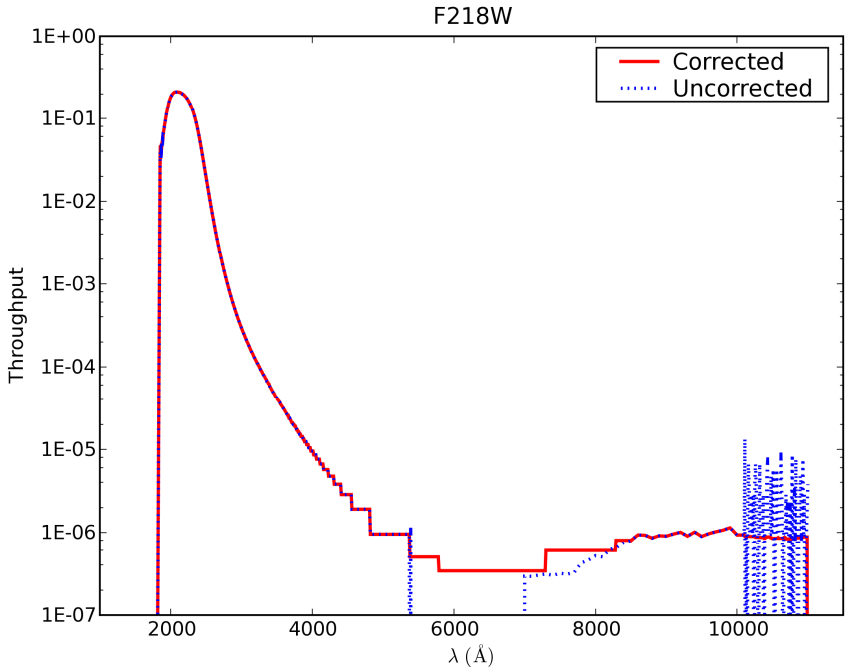


**Figure 10:** Previously available (blue dotted line; *wfpc2_f255w_006_syn.fits*) and corrected (red solid line; *wfpc2_f255w_007_syn.fits*) throughputs for F255W.

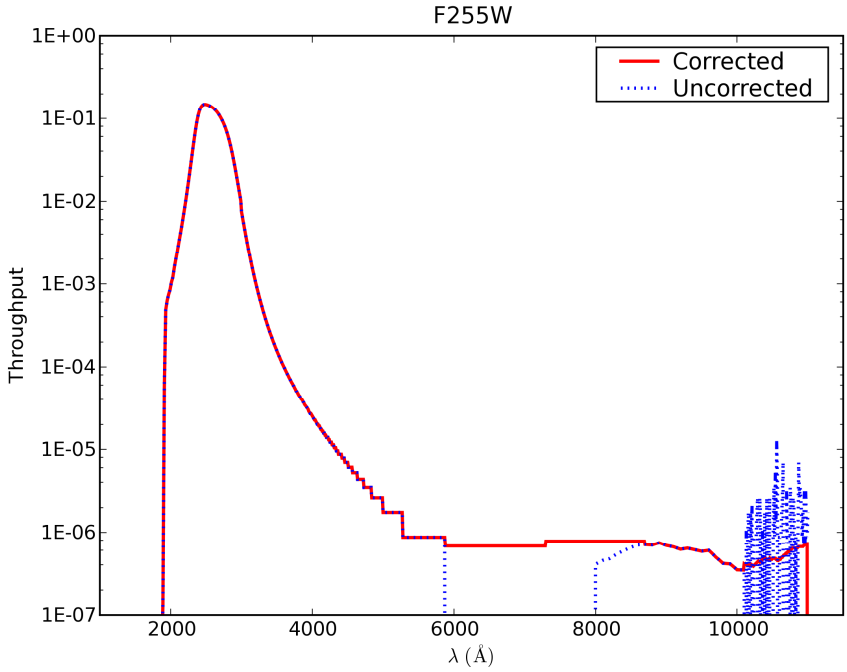

Comparisons of our revised red leak throughputs for these two filters with those in the WFPC2 Science Calibration Report (Trauger et al. 1993) show our revised red leaks are a factor of 2 to 3 higher. This could be attributed to growth of pinholes, different measurement methods, etc.

### 5.6.5. F170W, F300W, and F336W

The agreements for red leak fluxes between observations and SYNPHOT are satisfactory for F170W, F300W, and F336W. The F170W filter has $|\Delta f|$ values within 5% for both g Gem and 15 Mon, except F170W×F450W for 15 Mon with ~14% (some contributions from UV in-band fluxes and also more susceptible to blue leak in F450W, if any; see Section 4.2). Meanwhile, both F300W and F336W have $|\Delta f| \lesssim 20\%$ for 15 Mon (no data for g Gem). Therefore, we find it unnecessary to modify the existing throughput tables for these three UV filters.

## 6. New Off-Band to In-Band Flux Ratios

With the new SYNPHOT throughput files for F185W, F218W, and F255W (see Sections 5.6.3 and 5.6.4) and other CDBS modifications over the years, there is a need to update Table 3.13 in the IHB (version 10.0).

Hence, we recalculated the percentage red leaks for the 71 BPGS stellar spectra and tabulated them in Table 4. As described in IHB Section 3.8, this table estimates the red leak, if any, for a given UV filter and spectral type as the percentage of the detected flux long-ward of the cutoff wavelength in the third header row. For instance, when an O5-type star is observed with F300W, 0.5% of the total flux would come from the red leak region long-ward of 3800 Å.

Comparing Table 4 with its predecessor, Table 3.13 in IHB v. 10.0, the columns associated with F185W, F218W, and F255W have changed as much as 20.5% (G8V), 8.2% (M0V), and 10.0% (M6V), respectively. Changes for the other five UV filters, if any, are <0.1%.

**Table 4:** Percentage red leak in UV filters for different cutoff wavelengths. A synthetic photometry calculation with de-reddened BPGS stellar spectra and system response from on-orbit data. This table supersedes Table 3.13 in IHB (v. 10.0).

| Filter | | F122M | F160BW | F170W | F185W | F218W | F255W | F300W | F336W | F122M | F160BW | F170W | F185W | F218W | F255W | F300W | F336W |
|---|---|---|---|---|---|---|---|---|---|---|---|---|---|---|---|---|---|
| Central λ (nm) | | 122 | 160 | 170 | 185 | 218 | 255 | 300 | 336 | 122 | 160 | 170 | 185 | 218 | 255 | 300 | 336 |
| Cutoff λ (nm) | | 140 | 240 | 260 | 260 | 280 | 310 | 400 | 400 | 380 | 380 | 380 | 380 | 380 | 380 | 380 | 380 |
| 9 SGR | O5 | 17.1 | — | 0.7 | 0.4 | 0.2 | 0.3 | — | 0.1 | 0.3 | — | 0.1 | — | — | — | 0.5 | 0.1 |
| 9 SGE | O8F | 17.1 | — | 0.7 | 0.4 | 0.2 | 0.3 | — | 0.1 | 0.3 | — | 0.1 | — | — | — | 0.5 | 0.1 |
| HR 8023 | O6 | 22.0 | — | 1.0 | 0.5 | 0.3 | 0.4 | — | 0.1 | 0.6 | — | 0.1 | — | — | — | 0.5 | 0.1 |
| BD -01 935 | B1V | 20.3 | — | 0.8 | 0.4 | 0.3 | 0.4 | — | 0.1 | 0.5 | — | 0.1 | — | — | — | 0.6 | 0.1 |
| 60 CYG | B1V | 20.3 | — | 0.8 | 0.4 | 0.3 | 0.4 | — | 0.1 | 0.6 | — | 0.1 | — | — | — | 0.6 | 0.1 |
| 102 HER | B2V | 22.8 | — | 1.2 | 0.6 | 0.4 | 0.5 | 0.1 | 0.1 | 1.1 | — | 0.2 | — | — | — | 0.7 | 0.2 |
| ETA HYA | B3V | 23.0 | — | 1.2 | 0.6 | 0.4 | 0.5 | 0.1 | 0.1 | 1.3 | — | 0.3 | 0.1 | — | — | 0.8 | 0.2 |
| IOTA HER | B3V | 23.0 | — | 1.2 | 0.6 | 0.4 | 0.5 | 0.1 | 0.1 | 1.3 | — | 0.3 | 0.1 | — | — | 0.8 | 0.2 |
| HR 7899 | B4V | 23.0 | — | 1.2 | 0.6 | 0.4 | 0.5 | 0.1 | 0.1 | 1.3 | — | 0.3 | 0.1 | — | — | 0.8 | 0.2 |
| 38 OPH | A1V | 30.3 | — | 1.6 | 0.7 | 0.5 | 0.5 | 0.1 | 0.2 | 2.9 | — | 0.5 | 0.1 | — | — | 1.0 | 0.3 |
| HR 7174 | B6V | 31.0 | — | 1.8 | 0.8 | 0.5 | 0.6 | 0.1 | 0.3 | 3.7 | — | 0.6 | 0.1 | — | 0.1 | 1.3 | 0.4 |
| 9 VUL | B7V | 31.1 | — | 1.8 | 0.8 | 0.5 | 0.6 | 0.1 | 0.3 | 3.9 | — | 0.7 | 0.1 | — | 0.1 | 1.3 | 0.4 |
| HD 189689 | B9V | 41.3 | — | 2.4 | 0.9 | 0.5 | 0.6 | 0.2 | 0.3 | 7.3 | — | 1.0 | 0.2 | — | 0.1 | 1.6 | 0.4 |
| THETA VIR | A0V | 59.5 | — | 4.0 | 1.2 | 0.6 | 0.8 | 0.3 | 0.5 | 20.0 | — | 2.2 | 0.4 | 0.1 | 0.2 | 2.4 | 0.7 |
| NU CAP | B9V | 58.5 | — | 3.7 | 1.1 | 0.6 | 0.8 | 0.3 | 0.5 | 18.0 | — | 1.9 | 0.3 | 0.1 | 0.1 | 2.1 | 0.6 |
| HR 6169 | A2V | 59.4 | — | 4.0 | 1.2 | 0.6 | 0.8 | 0.3 | 0.5 | 19.8 | — | 2.2 | 0.4 | 0.1 | 0.1 | 2.2 | 0.6 |
| HD 190849A | A1V | 73.3 | — | 3.8 | 1.1 | 0.6 | 0.8 | 0.3 | 0.5 | 23.2 | — | 2.0 | 0.3 | 0.1 | 0.1 | 1.9 | 0.6 |
| 69 HER | A2V | 59.4 | — | 3.9 | 1.1 | 0.6 | 0.8 | 0.3 | 0.5 | 19.7 | — | 2.2 | 0.4 | 0.1 | 0.1 | 2.1 | 0.7 |
| HD 190849B | A3V | 88.7 | — | 6.5 | 1.5 | 0.8 | 1.0 | 0.3 | 0.6 | 43.6 | — | 3.8 | 0.5 | 0.1 | 0.2 | 2.3 | 0.7 |
| 58 AQL | A0V | 75.1 | — | 4.3 | 1.2 | 0.6 | 0.8 | 0.3 | 0.7 | 28.1 | — | 2.5 | 0.4 | 0.1 | 0.2 | 2.6 | 0.8 |
| 78 HER | B9V | 74.6 | — | 4.2 | 1.2 | 0.6 | 0.8 | 0.3 | 0.6 | 27.0 | — | 2.4 | 0.4 | 0.1 | 0.1 | 2.3 | 0.7 |
| HR 6570 | A7V | 89.4 | — | 7.0 | 1.5 | 0.8 | 1.1 | 0.4 | 0.7 | 47.1 | — | 4.4 | 0.6 | 0.1 | 0.2 | 2.5 | 0.8 |
| HD 187754 | A2V | 97.9 | — | 11.0 | 2.0 | 1.0 | 1.2 | 0.5 | 0.9 | 64.2 | — | 7.4 | 0.9 | 0.2 | 0.3 | 3.1 | 1.0 |
| THETA 1 SER | A5V | 97.6 | — | 9.9 | 1.9 | 0.9 | 1.2 | 0.4 | 0.7 | 60.0 | — | 6.2 | 0.7 | 0.2 | 0.2 | 2.5 | 0.8 |
| PRAESEPE 276 | | 99.7 | — | 12.2 | 2.1 | 1.0 | 1.3 | 0.5 | 0.9 | 67.3 | — | 8.1 | 0.9 | 0.2 | 0.3 | 2.8 | 1.0 |
| PRAESEPE 114 | | 99.7 | — | 11.7 | 2.1 | 1.0 | 1.2 | 0.5 | 0.8 | 65.9 | — | 7.6 | 0.9 | 0.2 | 0.2 | 2.6 | 0.9 |
| PRAESEPE 154 | | 100.0 | — | 17.3 | 2.8 | 1.2 | 1.4 | 0.5 | 0.8 | 71.8 | — | 11.5 | 1.2 | 0.2 | 0.3 | 2.7 | 0.9 |
| HD 190192 | A5V | 100.0 | — | 17.6 | 2.9 | 1.2 | 1.4 | 0.5 | 0.9 | 72.5 | — | 11.8 | 1.3 | 0.2 | 0.3 | 2.7 | 1.0 |
| PRAESEPE 226 | | 100.0 | — | 17.5 | 2.9 | 1.2 | 1.4 | 0.5 | 0.9 | 72.5 | — | 11.7 | 1.3 | 0.2 | 0.3 | 2.5 | 1.0 |
| PRAESEPE 37 | | 100.0 | — | 39.1 | 7.4 | 2.1 | 1.9 | 0.6 | 0.9 | 80.6 | — | 27.0 | 3.5 | 0.4 | 0.3 | 2.7 | 1.0 |
| HD 191177 | F4V | 100.0 | — | 65.2 | 16.8 | 3.2 | 2.5 | 0.8 | 1.1 | 85.9 | — | 48.3 | 9.1 | 0.7 | 0.5 | 3.4 | 1.2 |
| PRAESEPE 332 | | 100.0 | — | 62.7 | 15.8 | 3.0 | 2.4 | 0.7 | 1.0 | 84.4 | — | 44.8 | 8.0 | 0.6 | 0.4 | 2.7 | 1.1 |
| BD +29 3891 | F6V | 100.0 | — | 67.7 | 18.9 | 3.9 | 2.7 | 0.8 | 1.1 | 86.2 | — | 49.7 | 10.2 | 0.8 | 0.5 | 2.9 | 1.2 |
| PRAESEPE 222 | | 100.0 | — | 51.1 | 11.2 | 3.0 | 2.4 | 0.7 | 1.1 | 84.5 | — | 36.8 | 5.8 | 0.6 | 0.4 | 2.6 | 1.1 |
| HD 35296 | F8V | 100.0 | — | 52.5 | 11.7 | 3.0 | 2.4 | 0.8 | 1.2 | 85.7 | — | 38.7 | 6.3 | 0.6 | 0.4 | 2.7 | 1.3 |
| BD +26 3780 | G0V | 100.0 | — | 52.8 | 11.8 | 3.0 | 2.4 | 0.8 | 1.2 | 85.8 | — | 39.0 | 6.4 | 0.6 | 0.4 | 2.7 | 1.3 |
| HD 148816 | F9V | 100.0 | — | 51.5 | 11.4 | 3.0 | 2.4 | 0.8 | 1.1 | 84.9 | — | 37.3 | 6.0 | 0.6 | 0.4 | 2.7 | 1.2 |
| HD 155675 | F8V | 100.0 | — | 69.4 | 20.2 | 5.0 | 3.7 | 0.9 | 1.2 | 88.5 | — | 53.2 | 11.9 | 1.2 | 0.7 | 3.1 | 1.3 |
| PRAESEPE 418 | | 100.0 | — | 70.5 | 20.8 | 5.1 | 3.8 | 1.0 | 1.3 | 89.2 | — | 55.0 | 12.6 | 1.2 | 0.7 | 3.0 | 1.4 |
| HYAD 1 | | 100.0 | — | 71.7 | 21.6 | 5.2 | 3.8 | 1.1 | 1.4 | 89.8 | — | 56.7 | 13.5 | 1.3 | 0.8 | 3.2 | 1.5 |
| HD 122693 | F8V | 100.0 | — | 71.9 | 21.8 | 5.2 | 3.8 | 1.1 | 1.5 | 89.9 | — | 57.0 | 13.6 | 1.3 | 0.8 | 3.3 | 1.6 |
| HD 154417 | F8V | 100.0 | — | 70.9 | 21.1 | 5.1 | 3.8 | 1.0 | 1.4 | 89.3 | — | 55.5 | 12.9 | 1.2 | 0.7 | 3.1 | 1.4 |
| HYAD 2 | | 100.0 | — | 89.4 | 46.3 | 8.5 | 3.8 | 1.2 | 1.6 | 91.1 | — | 71.3 | 29.3 | 2.1 | 0.8 | 3.1 | 1.6 |
| HD 227547 | G5V | 100.0 | — | 89.6 | 46.7 | 8.6 | 3.8 | 1.2 | 1.6 | 91.2 | — | 71.7 | 29.8 | 2.2 | 0.8 | 3.2 | 1.7 |
| HD 154760 | G2V | 100.0 | — | 89.4 | 46.4 | 8.5 | 3.7 | 1.2 | 1.6 | 91.1 | — | 71.3 | 29.4 | 2.1 | 0.8 | 3.2 | 1.6 |
| HD 190605 | G2V | 100.0 | — | 90.0 | 47.7 | 8.7 | 3.8 | 1.3 | 1.7 | 91.7 | — | 72.9 | 31.1 | 2.3 | 0.8 | 3.2 | 1.8 |
| HYAD 15 | | 100.0 | — | 90.2 | 48.1 | 8.7 | 3.8 | 1.3 | 1.7 | 91.9 | — | 73.4 | 31.6 | 2.3 | 0.8 | 3.2 | 1.8 |
| HD 139777A | K0V | 100.0 | — | 89.9 | 47.5 | 8.6 | 3.8 | 1.3 | 1.7 | 91.6 | — | 72.5 | 30.7 | 2.2 | 0.8 | 3.3 | 1.8 |
| HD 136274 | G8V | 100.0 | — | 91.5 | 51.5 | 9.0 | 3.9 | 1.6 | 2.2 | 93.2 | — | 76.9 | 36.1 | 2.6 | 0.9 | 3.4 | 2.3 |
| HYAD 26 | | 100.0 | — | 91.7 | 52.1 | 9.1 | 4.0 | 1.6 | 2.2 | 93.4 | — | 77.4 | 36.7 | 2.7 | 1.0 | 3.4 | 2.3 |
| HD 150205 | G5V | 100.0 | — | 91.7 | 52.2 | 9.1 | 3.9 | 1.7 | 2.2 | 93.4 | — | 77.4 | 36.8 | 2.7 | 1.0 | 3.6 | 2.3 |
| HYAD 21 | | 100.0 | — | 92.9 | 55.8 | 9.6 | 4.1 | 2.0 | 2.7 | 94.5 | — | 80.5 | 41.5 | 3.2 | 1.1 | 3.7 | 2.7 |
| BD +02 3001 | G8V | 100.0 | — | 93.0 | 56.4 | 9.5 | 4.1 | 2.1 | 2.9 | 94.7 | — | 80.9 | 42.3 | 3.2 | 1.1 | 4.1 | 3.0 |
| HD 190571 | G8V | 100.0 | 0.3 | 99.5 | 95.3 | 43.9 | 12.7 | 3.3 | 3.4 | 96.6 | 0.1 | 91.1 | 80.1 | 20.5 | 4.0 | 5.8 | 3.5 |
| HYAD 183 | | 100.0 | 0.3 | 99.6 | 96.1 | 46.1 | 13.4 | 4.1 | 4.4 | 97.4 | 0.1 | 92.9 | 83.7 | 23.7 | 4.7 | 6.4 | 4.4 |
| HD 190470 | K3V | 100.0 | 0.4 | 99.6 | 96.3 | 46.9 | 13.6 | 4.3 | 4.6 | 97.5 | 0.1 | 93.2 | 84.3 | 24.6 | 4.9 | 6.6 | 4.6 |
| HD 154712 | K4V | 100.0 | 0.1 | 99.7 | 95.8 | 51.3 | 18.4 | 6.4 | 6.3 | 98.3 | 0.1 | 95.1 | 87.5 | 31.5 | 7.7 | 8.9 | 6.4 |
| HYAD 185 | | 100.0 | 0.2 | 99.7 | 96.9 | 56.2 | 18.6 | 7.7 | 7.5 | 98.5 | 0.1 | 95.9 | 89.8 | 36.5 | 8.2 | 10.1 | 7.6 |
| BD +38 2457 | K8V | 100.0 | 0.2 | 99.7 | 96.7 | 55.0 | 19.8 | 8.5 | 8.6 | 98.7 | 0.1 | 96.3 | 90.3 | 36.9 | 9.4 | 11.0 | 8.6 |
| HYAD 173 | | 100.0 | 0.1 | 99.5 | 94.3 | 38.3 | 11.0 | 11.4 | 12.1 | 99.0 | — | 96.9 | 89.4 | 26.8 | 6.1 | 13.8 | 12.2 |
| GL 40 | M0V | 100.0 | 0.1 | 99.6 | 95.3 | 41.3 | 11.8 | 14.0 | 14.7 | 99.2 | — | 97.4 | 91.3 | 30.4 | 7.0 | 16.8 | 14.8 |
| HYAD 189 | | 100.0 | 0.1 | 99.6 | 95.8 | 42.9 | 12.3 | 15.2 | 15.9 | 99.3 | — | 97.7 | 92.1 | 32.3 | 7.5 | 17.7 | 16.0 |
| HD 151288 | K7V | 100.0 | 0.1 | 99.7 | 96.0 | 44.3 | 12.8 | 16.0 | 16.5 | 99.3 | — | 97.8 | 92.5 | 33.7 | 8.0 | 18.6 | 16.6 |
| HD 157881 | K7V | 100.0 | 0.1 | 99.7 | 96.0 | 43.8 | 12.5 | 16.2 | 16.7 | 99.3 | — | 97.8 | 92.5 | 33.3 | 7.8 | 18.8 | 16.8 |
| HD 132683 | M0V | 100.0 | 0.1 | 99.7 | 96.2 | 44.8 | 12.9 | 17.2 | 18.0 | 99.4 | — | 97.9 | 92.9 | 34.5 | 8.1 | 19.8 | 18.0 |
| GL 15A | M0V | 100.0 | 0.1 | 99.8 | 98.0 | 56.0 | 16.9 | 26.7 | 25.6 | 99.6 | 0.1 | 98.8 | 96.1 | 47.4 | 12.1 | 29.6 | 25.7 |
| GL 49 | M2V | 100.0 | 0.1 | 99.8 | 97.7 | 53.0 | 15.4 | 24.8 | 23.9 | 99.6 | 0.1 | 98.7 | 95.6 | 44.1 | 10.8 | 27.8 | 24.0 |
| GL 109 | M4V | 100.0 | 0.1 | 99.9 | 98.5 | 61.0 | 18.6 | 33.5 | 31.0 | 99.7 | 0.1 | 99.1 | 97.1 | 53.6 | 14.2 | 36.4 | 31.1 |
| GL 15B | M6V | 100.0 | 0.2 | 99.9 | 99.3 | 74.8 | 27.6 | 50.4 | 44.6 | 99.9 | 0.1 | 99.6 | 98.6 | 69.9 | 23.5 | 52.7 | 44.7 |
| GL 83.1 | M8V | 100.0 | 0.1 | 99.7 | 96.4 | 43.7 | 12.0 | 16.7 | 14.5 | 99.4 | — | 97.9 | 93.2 | 32.7 | 6.8 | 19.2 | 14.6 |
| GL 65 | M5V | 100.0 | 0.1 | 99.8 | 97.4 | 48.0 | 12.5 | 21.6 | 16.7 | 99.6 | — | 98.5 | 95.1 | 38.2 | 7.5 | 24.2 | 16.8 |

## 7. Summary

As part of a WFPC2 close-out calibration project, we observed 15 Mon (an O7Ve-type star) and g Gem (a K4III-type star) to characterize red leak properties of eight UV filters by crossing them with three "red" filters (F450W, F606W, and F814W). Exposures of 15 Mon were done in five pointings to test for filter inhomogeneities.

The F170W, F300W, and F336W filters showed good agreement between the predicted (SYNPHOT) and measured red leaks. The F160BW filter had undetectable red leaks in all three crossing filters for both 15 Mon and follow-up observations of Antares.

There was poor agreement between the predicted and measured red leaks for F185W, F218W, and F255W. One source of inconsistency was the presence of "gaps" in the SYNPHOT throughput curves for these filters. We empirically filled these gaps using the g Gem and 15 Mon data. We also removed throughput digitization effects at $\lambda \gtrsim$ 10,000 Å for these three filters. Their in-band transmissions were confirmed to be unaffected by checking the new throughputs against GRW+70 5824 exposures without crossing filters. We delivered these three new SYNPHOT throughput files to CDBS and recalculated percentage red leaks to replace Table 3.13 in IHB (v. 10.0).

Observed count rates in the F122M filter were significantly lower than predicted by SYNPHOT, which we attribute to a long-term transmission decline. We further investigated this issue using exposures from calibration star GRW+70 5824 and found an overall throughput deterioration of ~19%, which is consistent with that found in the SIC&DH post-recovery report (Biretta & Gonzaga 2008; private communications). Detailed studies of this filter are left to the future.

No filter inhomogeneities were detected, and should not exceed 5% of the measured red leaks. For situations with weak red leaks, some differences were found between the centers of the WF2 and WF3 CCDs; however, we argue these are attributable to chip-dependent CTE effects rather than filter inhomogeneity. We found no correlation between contamination effects and our measured red leaks, which was expected given that our signals were dominated by long wavelengths.

## Acknowledgements

We are grateful to Dr. John MacKenty and Dr. Jesús M. Apellániz (IAA, Spain) for helpful discussions on the F160BW red leak issue. We also thank Dr. Ralph Bohlin, who reviewed this report and provided insightful feedback.

## References


Anderson, J., & King, I. R. 1999, PASP, 111, 1095

Baggett, S., Casertano, S., Gonzaga, S., & Ritchie, C. 1997, "WFPC2 Synphot Update," WFPC2 Instrument Science Report 97-10

Baggett, S., et al. 2002, in HST WFPC2 Data Handbook, v. 4.0, ed. B. Mobasher, Baltimore, STScI

Biretta, J., & Gonzaga, S. 2005, "Early Assessment of the WF4 Anomaly," WFPC2 Instrument Science Report 05-02

Biretta, J., & Kozhurina-Platais, V. 2005, "Hot Pixels as a Probe of WFPC2 CTE Effects," WFPC2 Instrument Science Report 05-01

Cawley, L., Goudfrooij, P., Whitmore, B., & Stiavelli, M. 2001, "HST CCD Performance in the Second Decade: Charge Transfer Efficiency," WFC3 Instrument Science Report 01-05

Chiaberge, M., & Sirianni, M. 2007, "ACS CCDs UV and narrowband filters red leak check," ACS Instrument Science Report 07-03

Diaz, R. I., & Cracraft, M. 2008, "Assessment and Delivery of Reference Files," CDBS Technical Instrument Report 08-01

Dolphin, A. E. 2004, WFPC2 Calibration and CTE Correction Updates (December 2004), http://purcell.as.arizona.edu/wfpc2_calib/2004_12_20.html

Gies, D. R., et al. 1997, ApJ, 475, L49

Gonzaga, S. 2002, WFPC2 Data Analysis: A Tutorial, version 3.0, (Baltimore, STScI)

Gunn, J. E., & Stryker, L. L. 1983, ApJS, 52, 121

Koekemoer, A. M., Biretta, J., & Mack, J. 2002, "Updated WFPC2 Flatfield Reference Files for 1995 – 2001," WFPC2 Instrument Science Report 02-02

McMaster, M., Biretta, J., et al. 2008, WFPC2 Instrument Handbook, Version 10.0 (Baltimore: STScI)

Trauger, J. T., ed. 1993, "The WFPC2 Science Calibration Report," Pre-launch Version 1.2 [IDT[g] Calibration Report]

[g] Members of the Investigation Definition Team (IDT) were J. T. Trauger, C. J. Burrows, J. Clarke, D. Crisp, J. Gallagher, R. E. Griffiths, J. Hester, J. Hoessel, J. Holtzman, J. Mould, and J. A. Westphal.

## Appendix A: Photometry Results for 15 Mon and g Gem

This section contains detailed photometry results discussed in Sections 5.1 and 5.2.

Reduced cross-filter images for 15 Mon and g Gem are shown in Figure A1 to Figure A6 – They are grouped by stars and "red" filters, with the UV filters labeled accordingly. WF3s pointing is shown as a representative although PSFs might vary slightly for the other pointings. Magenta circles mark their respective 2″ apertures, which effectively contain all the flux.

Aperture corrections (ΔMAG) are shown in Figure A7 and Figure A8 for 15 Mon and g Gem, respectively – They are separated by pointings and plotted across UV filters. Blue circles, olive green diamonds, and red asterisks represent crossing with F450W, F606W, and F814W, respectively. ΔMAG is the magnitude derived from a 0.5″ aperture subtracted from that of 2″; it is also $\Delta m_{ap}$ in Table A1 unless stated otherwise in the table footnotes. For calculations involving two apertures at the same chip location, no CTE correction is necessary. Errors shown reflect those derived from photometry (IRAF task *phot*) with statistical propagation.

Table A1 tabulates the main photometry results for 15 Mon (separated by pointings) and g Gem (WF3s only) – For each filter pair, the final count rate used is $f_{obs}$, which is the average of values corrected and uncorrected for CTE loss for center pointings and just the latter for side pointings. The raw magnitude measured for a 0.5″ aperture and its uncertainty are $m$ and $\delta m$, respectively. The aperture and CTE loss corrections, in magnitudes, are $\Delta m_{ap}$ and $\Delta m_{CTE}$, respectively. Several special cases are as indicated by the table footnotes.

**Figure A1:** Images of 15 Mon for UV filters crossed with F450W. Only WF3s pointing is shown. The respective UV filter name is labeled on the image. Its further companion could be seen 3″ away. Magenta circles mark their respective 2″ apertures.

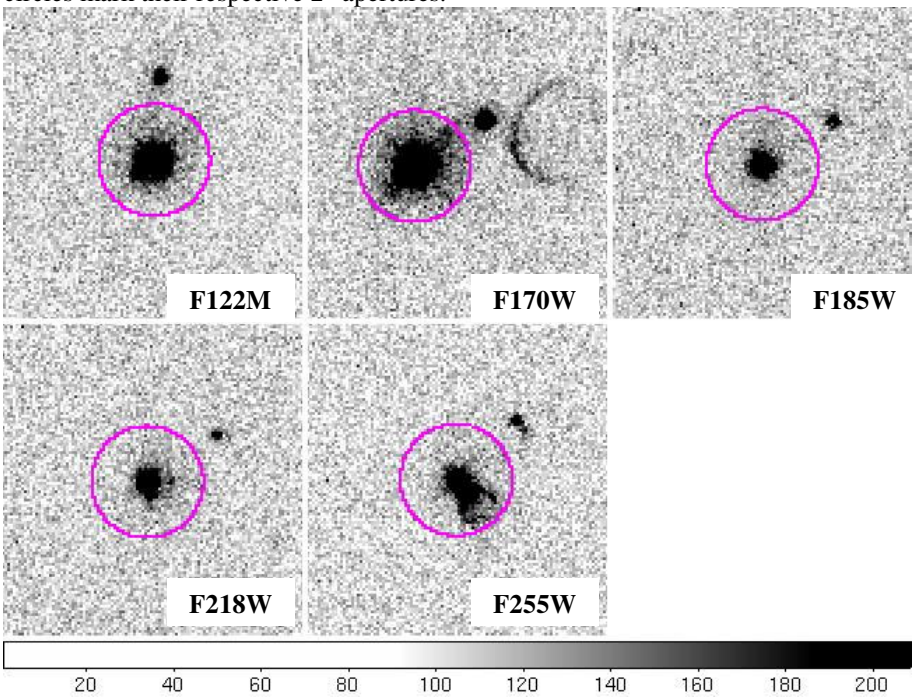


**Figure A2:** Images of 15 Mon for UV filters crossed with F606W. Only WF3s pointing is shown. The respective UV filter name is labeled on the image. Its further companion could be seen 3″ away, barely visible in F218W and F255W cross-filters. Magenta circles mark their respective 2″ apertures.

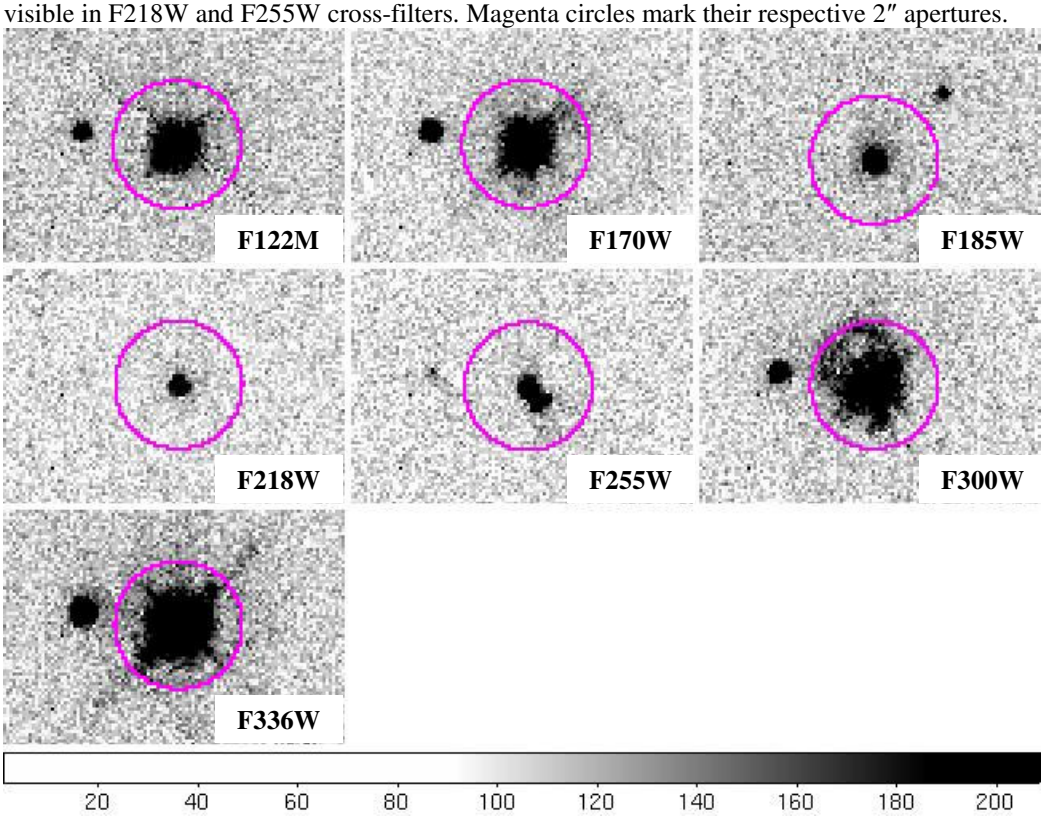

**Figure A3:** Images of 15 Mon for UV filters crossed with F814W. Only WF3s pointing is shown. The respective UV filter name is labeled on the image. Its further companion could be seen 3″ away, too faint to be seen in F218W and F255W cross-filters. Magenta circles mark their respective 2″ apertures.

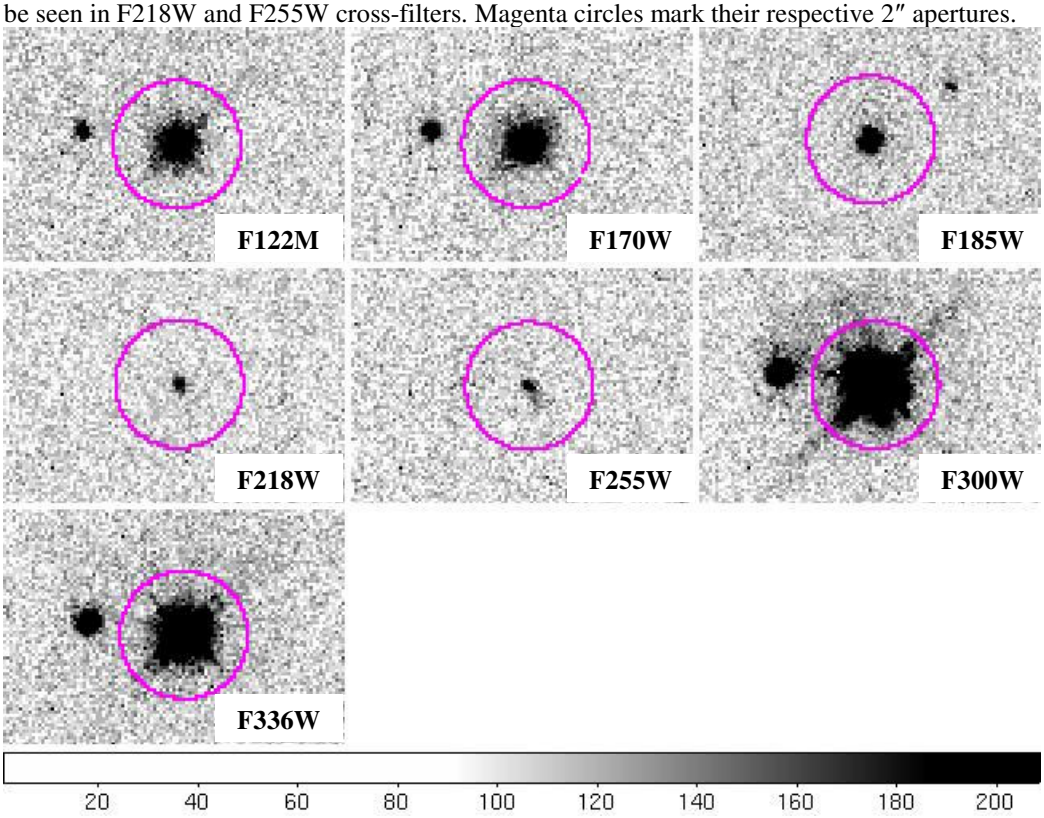


**Figure A4:** Images of g Gem for UV filters crossed with F450W. Only WF3s pointing is available. The respective UV filter name is labeled on the image. Magenta circles mark their respective 2″ apertures.

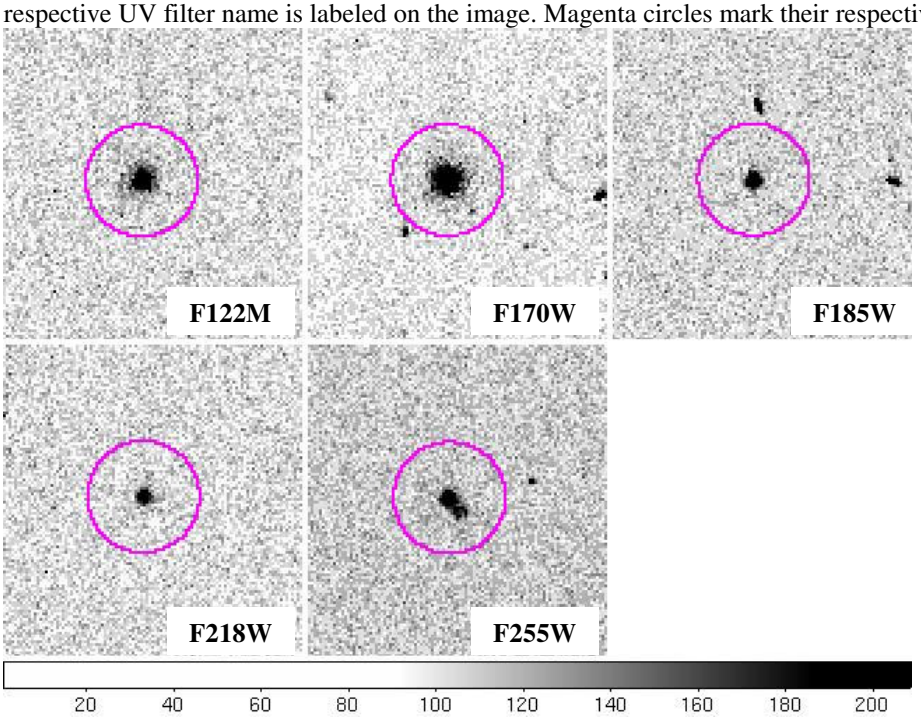

**Figure A5:** Images of g Gem for UV filters crossed with F606W. Only WF3s pointing is available. The respective UV filter name is labeled on the image. Magenta circles mark their respective 2″ apertures.

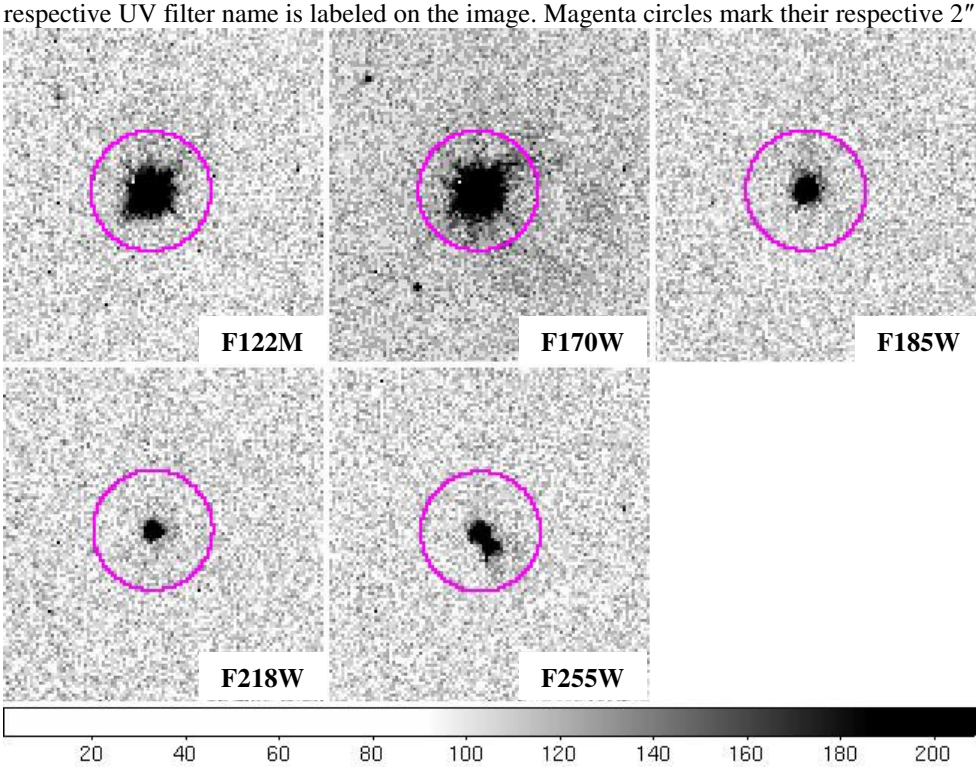


**Figure A6:** Images of g Gem for UV filters crossed with F814W. Only WF3s pointing is available. The respective UV filter name is labeled on the image. Magenta circles mark their respective 2″ apertures.

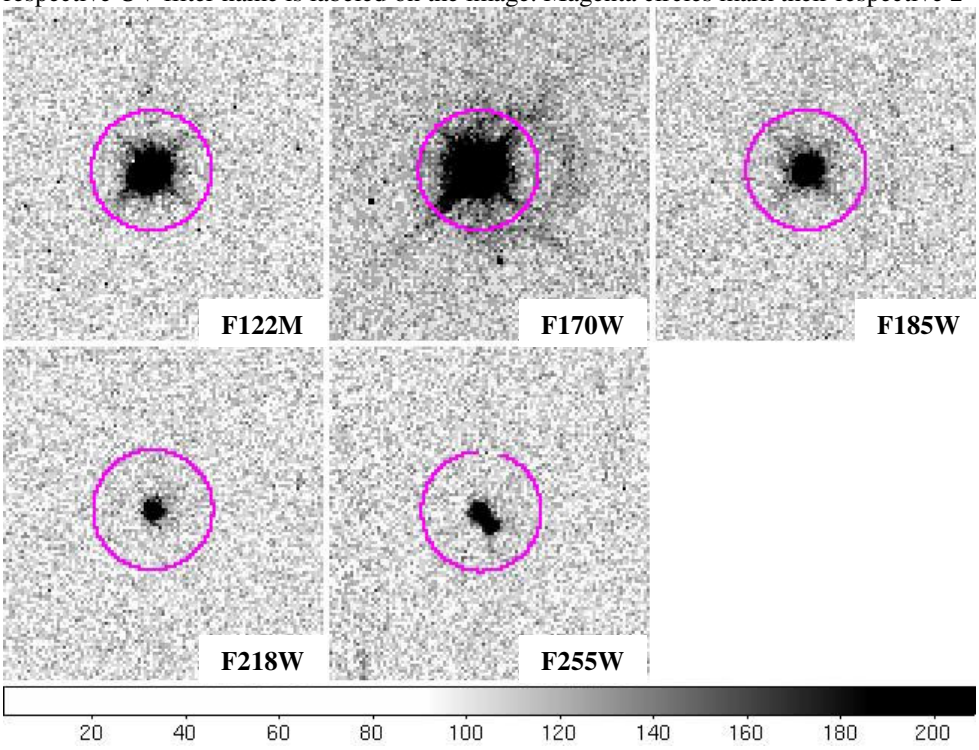

**Figure A7:** Aperture corrections for 15 Mon, i.e., 0.5″ aperture magnitude subtracted from that of 2″ (without CTE loss correction). These are equivalent to $\Delta m_{ap}$ in Table A1 unless stated otherwise in the table footnotes. Errors are statistically propagated from photometry results.

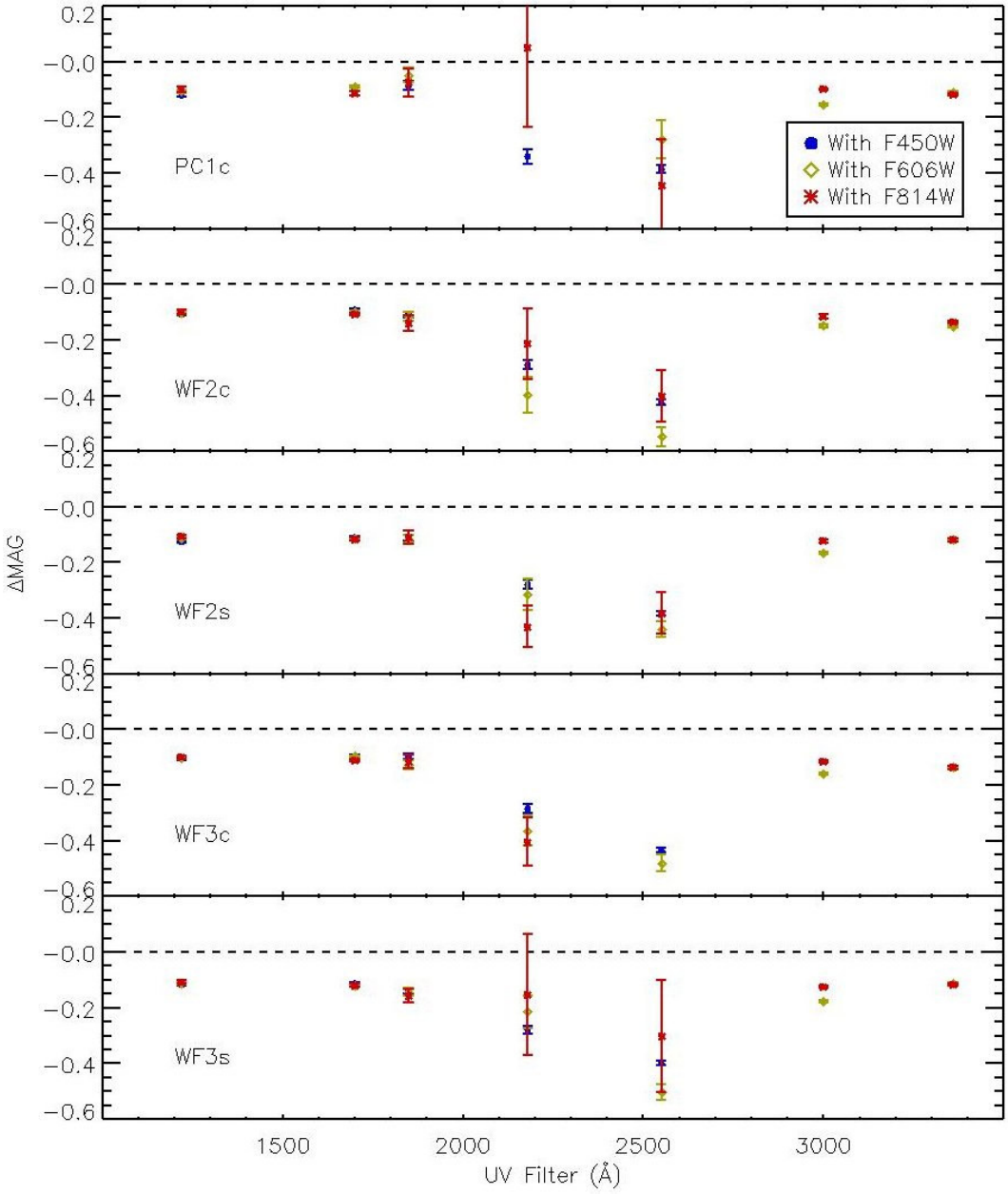


**Figure A8:** Same as Figure A7 but for g Gem.

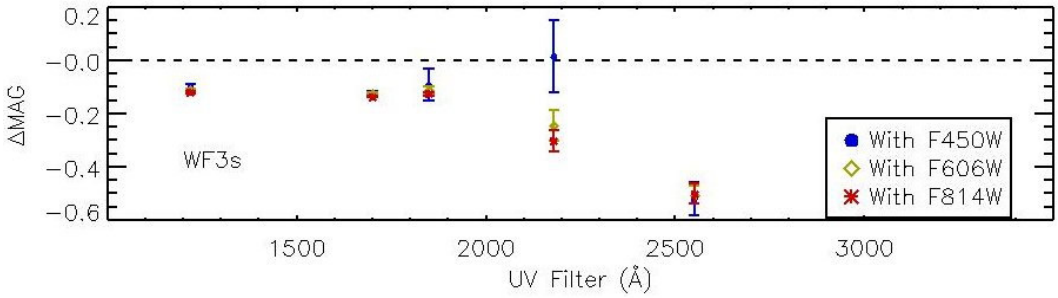

**Table A1:** Photometry results for 15 Mon and g Gem. The final count rate used is $f_{obs}$ (DN $s^{-1}$) – For the pointing at the center of the chip, it is the average of values corrected and uncorrected for CTE loss; for the pointing at the side, it is uncorrected for CTE loss. The raw magnitude measured for a 0.5″ aperture (uncorrected for CTE loss) and its uncertainty are $m$ and $\delta m$, respectively. The aperture and CTE loss corrections, in magnitudes, are $\Delta m_{ap}$ and $\Delta m_{CTE}$, respectively. See Sections 5.1 and 5.2 for full details.

| UV Filter | "Red" Filter | $f_{obs}$ | $m$ | $\delta m$ | $\Delta m_{ap}$ | $\Delta m_{CTE}$ |
|---|---|---|---|---|---|---|
| **Star: 15 Mon; Pointing: PC1c** | | | | | | |
| F122M | F450W | 278.02 | -5.929 | 0.003 | -0.121 | -0.116 |
| F122M | F606W | 276.22 | -5.937 | 0.003 | -0.107 | -0.115 |
| F122M | F814W | 154.10 | -5.304 | 0.004 | -0.100 | -0.127 |
| F170W | F450W | 580.44 | -6.764 | 0.002 | -0.092 | -0.105 |
| F170W | F606W | 443.75 | -6.471 | 0.002 | -0.091 | -0.109 |
| F170W | F814W | 197.78 | -5.564 | 0.004 | -0.114 | -0.122 |
| F185W | F450W | 83.65 | -4.647 | 0.007 | -0.086 | -0.142 |
| F185W | F606W | 49.68 | -4.110 | 0.009 | -0.048 | -0.158 |
| F185W | F814W | 26.50 | -3.386 | 0.016 | -0.075 | -0.186 |
| F218W | F450W | 49.44 | -3.806 | 0.011 | -0.341 | -0.169 |
| F218W | F606W† | 9.94 | -2.009 | 0.047 | -0.341 | -0.270 |
| F218W | F814W† | 2.74 | -0.588 | 0.069 | -0.341 | -0.306 |
| F255W | F450W | 118.05 | -4.721 | 0.006 | -0.386 | -0.140 |
| F255W | F606W† | 21.11 | -2.811 | 0.024 | -0.386 | -0.215 |
| F255W | F814W† | 3.26 | -0.742 | 0.060 | -0.386 | -0.291 |
| F300W | F606W | 386.33 | -6.255 | 0.003 | -0.155 | -0.111 |
| F300W | F814W | 1043.07 | -7.395 | 0.002 | -0.100 | -0.099 |
| F336W | F606W | 1093.78 | -7.437 | 0.002 | -0.110 | -0.099 |
| F336W | F814W | 2247.68 | -8.204 | 0.002 | -0.118 | -0.112 |
| **Star: 15 Mon; Pointing: WF2c** | | | | | | |
| F122M | F450W | 302.63 | -6.037 | 0.003 | -0.108 | -0.113 |
| F122M | F606W | 296.97 | -6.021 | 0.003 | -0.103 | -0.113 |
| F122M | F814W | 165.67 | -5.385 | 0.004 | -0.100 | -0.124 |
| F170W | F450W | 641.53 | -6.874 | 0.002 | -0.092 | -0.103 |
| F170W | F606W | 482.23 | -6.555 | 0.002 | -0.099 | -0.106 |
| F170W | F814W | 212.26 | -5.649 | 0.003 | -0.107 | -0.119 |
| F185W | F450W | 80.27 | -4.578 | 0.006 | -0.110 | -0.141 |
| F185W | F606W | 46.88 | -3.981 | 0.008 | -0.114 | -0.160 |
| F185W | F814W | 25.30 | -3.270 | 0.012 | -0.140 | -0.187 |
| F218W | F450W | 44.20 | -3.736 | 0.009 | -0.289 | -0.170 |
| F218W | F606W† | 9.66 | -2.033 | 0.027 | -0.289 | -0.264 |
| F218W | F814W† | 2.32 | -0.454 | 0.041 | -0.289 | -0.315 |
| F255W | F450W | 119.15 | -4.693 | 0.006 | -0.425 | -0.139 |
| F255W | F606W† | 19.16 | -2.664 | 0.017 | -0.425 | -0.221 |
| F255W | F814W† | 3.05 | -0.625 | 0.036 | -0.425 | -0.299 |
| F300W | F606W | 381.89 | -6.248 | 0.003 | -0.150 | -0.110 |
| F300W | F814W | 1035.39 | -7.357 | 0.004 | -0.116 | -0.126 |
| F336W | F606W | 1099.89 | -7.389 | 0.004 | -0.152 | -0.123 |
| F336W | F814W | 2328.66 | -8.220 | 0.003 | -0.137 | -0.119 |
| **Star: 15 Mon; Pointing: WF2s** | | | | | | |
| F122M | F450W | 296.25 | -6.052 | 0.003 | -0.127 | — |
| F122M | F606W | 290.65 | -6.043 | 0.003 | -0.115 | — |
| F122M | F814W | 164.82 | -5.435 | 0.004 | -0.107 | — |
| F170W | F450W | 608.21 | -6.852 | 0.002 | -0.108 | — |
| F170W | F606W | 465.73 | -6.557 | 0.002 | -0.113 | — |
| F170W | F814W | 207.38 | -5.676 | 0.003 | -0.116 | — |
| F185W | F450W | 85.08 | -4.712 | 0.005 | -0.112 | — |
| F185W | F606W | 52.65 | -4.186 | 0.007 | -0.117 | — |
| F185W | F814W | 27.56 | -3.490 | 0.010 | -0.111 | — |
| F218W | F450W | 48.35 | -3.932 | 0.008 | -0.279 | — |
| F218W | F606W† | 10.76 | -2.301 | 0.022 | -0.279 | — |
| F218W | F814W† | 2.93 | -0.887 | 0.030 | -0.279 | — |

| UV Filter | "Red" Filter | $f_{obs}$ | $m$ | $\delta m$ | $\Delta m_{ap}$ | $\Delta m_{CTE}$ |
|---|---|---|---|---|---|---|
| F255W | F450W | 122.28 | -4.836 | 0.005 | -0.383 | — |
| F255W | F606W[†] | 23.16 | -3.029 | 0.014 | -0.383 | — |
| F255W | F814W[†] | 3.35 | -0.931 | 0.029 | -0.383 | — |
| F300W | F606W | 379.87 | -6.282 | 0.003 | -0.167 | — |
| F300W | F814W | 1015.31 | -7.394 | 0.004 | -0.122 | — |
| F336W | F606W | 1061.58 | -7.449 | 0.001 | -0.116 | — |
| F336W | F814W | 2282.05 | -8.277 | 0.003 | -0.119 | — |
| **Star: 15 Mon; Pointing: WF3c** | | | | | | |
| F122M | F450W | 318.14 | -6.094 | 0.003 | -0.105 | -0.113 |
| F122M | F606W | 324.43 | -6.119 | 0.003 | -0.101 | -0.112 |
| F122M | F814W | 178.91 | -5.469 | 0.004 | -0.100 | -0.123 |
| F170W | F450W | 631.69 | -6.853 | 0.002 | -0.095 | -0.104 |
| F170W | F606W | 493.79 | -6.583 | 0.002 | -0.096 | -0.107 |
| F170W | F814W | 215.91 | -5.663 | 0.003 | -0.111 | -0.120 |
| F185W | F450W | 82.34 | -4.619 | 0.006 | -0.096 | -0.143 |
| F185W | F606W | 52.76 | -4.098 | 0.008 | -0.127 | -0.156 |
| F185W | F814W | 28.88 | -3.441 | 0.011 | -0.116 | -0.182 |
| F218W | F450W | 48.39 | -3.841 | 0.009 | -0.285 | -0.166 |
| F218W | F606W[†] | 11.17 | -2.201 | 0.023 | -0.285 | -0.253 |
| F218W | F814W[†] | 2.85 | -0.695 | 0.034 | -0.285 | -0.295 |
| F255W | F450W | 120.53 | -4.696 | 0.006 | -0.434 | -0.141 |
| F255W | F606W[†] | 22.62 | -2.842 | 0.015 | -0.434 | -0.211 |
| F255W | F814W[†] | 3.83 | -0.876 | 0.029 | -0.434 | -0.279 |
| F300W | F606W | 407.22 | -6.307 | 0.003 | -0.161 | -0.111 |
| F300W | F814W | 1018.23 | -7.354 | 0.002 | -0.115 | -0.100 |
| F336W | F606W | 1109.40 | -7.428 | 0.002 | -0.134 | -0.099 |
| F336W | F814W | 2221.80 | -8.166 | 0.003 | -0.137 | -0.123 |
| **Star: 15 Mon; Pointing: WF3s** | | | | | | |
| F122M | F450W | 297.80 | -6.067 | 0.003 | -0.118 | — |
| F122M | F606W | 297.11 | -6.820 | 0.002 | -0.113 | — |
| F122M | F814W | 166.31 | -4.713 | 0.006 | -0.108 | — |
| F170W | F450W | 592.59 | -3.925 | 0.008 | -0.112 | — |
| F170W | F606W | 468.30 | -4.786 | 0.005 | -0.119 | — |
| F170W | F814W | 202.93 | -5.444 | 0.004 | -0.119 | — |
| F185W | F450W | 87.26 | -5.650 | 0.003 | -0.139 | — |
| F185W | F606W | 55.52 | -3.493 | 0.011 | -0.143 | — |
| F185W | F814W | 28.83 | -0.893 | 0.064 | -0.157 | — |
| F218W | F450W | 48.05 | -0.826 | 0.067 | -0.279 | — |
| F218W | F606W[†] | 11.30 | -7.428 | 0.002 | -0.279 | — |
| F218W | F814W[†] | 2.94 | -6.069 | 0.003 | -0.279 | — |
| F255W | F450W | 118.46 | -6.558 | 0.002 | -0.398 | — |
| F255W | F606W[†] | 22.52 | -4.218 | 0.007 | -0.398 | — |
| F255W | F814W[†] | 3.09 | -2.354 | 0.022 | -0.398 | — |
| F300W | F606W | 387.82 | -2.983 | 0.014 | -0.178 | — |
| F300W | F814W | 1049.89 | -6.294 | 0.003 | -0.125 | — |
| F336W | F606W | 1105.24 | -7.498 | 0.001 | -0.111 | — |
| F336W | F814W | 2271.26 | -8.275 | 0.002 | -0.116 | — |
| **Star: g Gem; Pointing: WF3s** | | | | | | |
| F122M | F450W | 60.23 | -4.346 | 0.007 | -0.104 | — |
| F122M | F606W | 368.74 | -6.304 | 0.003 | -0.112 | — |
| F122M | F814W | 839.18 | -7.190 | 0.003 | -0.119 | — |
| F170W | F450W | 115.36 | -5.030 | 0.005 | -0.126 | — |
| F170W | F606W | 556.80 | -6.739 | 0.003 | -0.125 | — |
| F170W | F814W | 990.28 | -7.352 | 0.002 | -0.137 | — |
| F185W | F450W | 14.67 | -2.824 | 0.023 | -0.092 | — |
| F185W | F606W | 62.17 | -4.373 | 0.007 | -0.111 | — |
| F185W | F814W | 151.13 | -5.323 | 0.004 | -0.125 | — |
| F218W | F450W[‡] | 5.70 | -1.588 | 0.037 | -0.301 | — |
| F218W | F606W | 10.81 | -2.341 | 0.022 | -0.244 | — |

| UV Filter | "Red" Filter | $f_{obs}$ | $m$ | $\delta m$ | $\Delta m_{ap}$ | $\Delta m_{CTE}$ |
|---|---|---|---|---|---|---|
| F218W | F814W | 15.54 | -2.678 | 0.017 | -0.301 | — |
| F255W | F450W | 14.70 | -2.399 | 0.029 | -0.520 | — |
| F255W | F606W | 20.50 | -2.774 | 0.016 | -0.505 | — |
| F255W | F814W | 18.07 | -2.641 | 0.018 | -0.501 | — |

† Aperture correction obtained from respective UV filter crossed with F450W.

‡ Using same aperture correction as F218W×F814W.

# Appendix B: SYNPHOT Results for 15 Mon and g Gem

Table B1 tabulates the predicted count rates ($f_{syn}$) from SYNPHOT for 15 Mon (PC1, WF2, and WF3) and g Gem (WF3 only), as described in Section 5.4. For F185W, F218W, and F255W, values from *uncorrected* throughputs are shown.

**Table B1:** SYNPHOT count rates in DN $s^{-1}$, $f_{syn}$, for 15 Mon (PC1, WF2, and WF3) and g Gem (WF3 only). Gain "7" is used, to be consistent with observations. Values for F185W, F218W, and F255W are from *uncorrected* throughputs. For g Gem, F300W and F336W values are not listed due to absence of corresponding observations.

| UV Filter | "Red" Filter | 15 Mon, PC1 | 15 Mon, WF2 | 15 Mon, WF3 | g Gem, WF3 |
|---|---|---|---|---|---|
| F122M | F450W | 477.15 | 486.09 | 490.59 | 97.95 |
| F122M | F606W | 494.93 | 508.82 | 499.78 | 626.78 |
| F122M | F814W | 236.94 | 241.21 | 243.39 | 1330.76 |
| F170W | F450W | 671.11 | 684.32 | 690.14 | 119.84 |
| F170W | F606W | 472.26 | 486.23 | 477.05 | 540.96 |
| F170W | F814W | 189.23 | 193.06 | 194.08 | 1033.66 |
| F185W | F450W | 107.15 | 110.09 | 109.95 | 11.86 |
| F185W | F606W | 18.42 | 20.37 | 18.19 | 0.03 |
| F185W | F814W | 14.03 | 14.57 | 14.41 | 64.02 |
| F218W | F450W | 61.89 | 63.95 | 63.37 | 5.54 |
| F218W | F606W | 16.41 | 17.61 | 16.43 | 3.35 |
| F218W | F814W | 6.41 | 6.84 | 6.44 | 12.58 |
| F255W | F450W | 136.69 | 139.49 | 140.82 | 13.44 |
| F255W | F606W | 16.23 | 16.67 | 16.51 | 9.24 |
| F255W | F814W | 2.35 | 2.45 | 2.41 | 6.62 |
| F300W | F606W | 356.25 | 369.84 | 356.32 | — |
| F300W | F814W | 913.24 | 940.65 | 923.70 | — |
| F336W | F606W | 1221.63 | 1268.06 | 1221.14 | — |
| F336W | F814W | 2385.52 | 2475.17 | 2387.25 | — |